Cell type specific control of basolateral amygdala plasticity via feedforward inhibition

E. Mae Guthman[1,2], Ming Ma[3], Philip Chu[2,4], Serapio M. Baca[2,5], Diego Restrepo[1,3#], Molly M. Huntsman[1,2,6*#]
[1] Neuroscience Graduate Program
[2]Department of Pharmaceutical Sciences
[3]Department of Cell and Developmental Biology
[4]Department of Neurosurgery
[5]Department of Neurology
[6]Department of Pediatrics
University of Colorado Anschutz Medical Campus, Aurora, CO 80045, USA

# D.R. and M.M.H. contributed equally to this work as senior authors.

*Corresponding author: Molly M. Huntsman, molly.huntsman@ucdenver.edu

The Author contributions: D.R. and M.M.H. supervised experiments; E.M.G., D.R., and M.M.H conceptualized and designed the experiments; E.M.G. conducted electrophysiology experiments; M.M. conducted and analyzed immunohistochemical experiments; E.M.G., P.C., and S.M.B. conceptualized and designed software for electrophysiological analyses; E.M.G and P.C. performed electrophysiological analyses; E.M.G. and M.M. created data visualizations; D.R. and M.M.H. provided resources; E.M.G wrote original draft. E.M.G., M.M., P.C., S.M.B., D.R., and M.M.H. read, edited, and wrote subsequent drafts of the manuscript.

Acknowledgments: We would like to thank Nicole Arevalo and the University of Colorado Anschutz Medical Campus Breeding Core for their assistance with animal care. We would also like to thank members of the Huntsman and Restrepo labs, Alicia M. Purkey, and Ashley M. Bourke for discussions on the data. This work was supported by U.S. National Institutes of Health grants (R01 DC000566 to D.R. and R01 NS095311 to M.M.H) and U.S. National Science Foundation Graduate Research Fellowship (DGE-1553798 to E.M.G.).

Abstract

The basolateral amygdala (BLA) plays a vital role in associating specific sensory stimuli with salient valence information. Excitatory principal neurons (PNs) undergo plastic changes to encode this integrated sensory-valence information; however, local BLA inhibitory interneurons (INs) gate the plasticity of the PNs via feed forward inhibition (FFI). Despite extensive literature implicating parvalbumin expressing (PV^+) INs in FFI in cortex and hippocampus, prior anatomical experiments in BLA implicate somatostatin expressing (Sst^+) INs in BLA. In the present study, we combined patch clamp electrophysiology with chemogenetics, unsupervised cluster analysis, and predictive modeling and found that a previously unreported subpopulation of fast-spiking Sst^+ INs mediate BLA FFI and gate plasticity.

44 The ability of animals to learn to associate sensory stimuli with outcomes plays an
45 important role in their survival. Specifically, animals associate environmental stimuli with
46 particular valences (rewarding or aversive outcomes). The BLA is key in formation of these
47 associations[1,2]. Following a small number of presentations of a stimulus and valence
48 information, such as a reward or threatening foot-shock, BLA excitatory PNs undergo plastic
49 changes. This plasticity is critically important as future presentations of the stimulus can then
50 elicit robust firing in subsets of BLA PNs that output to downstream regions to guide goal-
51 directed behavior[2-4].

52 Accumulating evidence demonstrates that this learning induced-plasticity is input-
53 specific[5-7]. Importantly, GABAergic inhibition regulates the ability of BLA PNs to undergo LTP:
54 plasticity does not occur in the presence of intact inhibition[8,9]. Specifically, FFI exerts
55 inhibitory control over BLA plasticity[8,10,11]. In cortex and hippocampus, FFI is mediated by
56 perisomatic targeting, PV^+ INs to ensure the temporal fidelity of PN action potential (AP)
57 output[12-14]. However, in BLA, FFI plays a dual role regulating PN AP output [15] and gating their
58 plasticity[10,11]. Which IN population mediates FFI to control plasticity in BLA remains unclear:
59 PV^+ INs are candidates because they mediate FFI in cortex and hippocampus[14,16], but
60 anatomical studies suggest that Sst^+ INs may play this role in the BLA[17,18].

61 Due to the role of dendritic inhibition in controlling local Ca^{2+} dynamics[19-21], the role of
62 postsynaptic Ca^{2+} dynamics in BLA plasticity[22-25], and the importance of FFI circuits in gating
63 BLA LTP[8,10,11], we hypothesized that Sst^+ INs gate FFI to control BLA plasticity. We tested this
64 hypothesis by pairing patch clamp recordings in BLA with chemogenetic manipulations,
65 unsupervised cluster analysis, and predictive modeling. We found that a previously unreported
66 subpopulation of fast spiking (FS) Sst^+ INs mediate FFI and gate plasticity in BLA.

67

68 **RESULTS**

69 **LEC afferents preferentially drive disynaptic FFI in BLA**

70 We examined lateral entorhinal cortex (LEC) afferents, a major cortical source of polysynaptic
71 inhibition to BLA[15]. We prepared acute horizontal slices of mouse brain containing both BLA
72 and LEC and recorded synaptic responses of BLA PNs (Figure 1a). A single stimulation of LEC
73 elicited evoked EPSCs (eEPSCs) and IPSCs (eIPSCs) in PNs (Figure 1b). The eEPSCs were
74 blocked by glutamate receptor antagonists DNQX (20 μM) and D-APV (50 μM) but not by the
75 $GABA_A$ receptor antagonist gabazine (gbz; 5 μM) (Figure 1c; median [quartiles]; $eEPSC_{control}$ = -
76 41.17 [-34.10/-51.47] pA, $eEPSC_{gbz}$ = -34.18 [-24.40/-39.23] pA, $eEPSC_{DNQX/APV}$ = -4.59 [-1.49/-
77 5.35] pA, $p = 6.72\times10^{-4}$, Kruskal-Wallis [KW] test, $p_{Ctrl\text{-}vs\text{-}gbz} = 0.19$, $p_{Ctrl\text{-}vs\text{-}DNQX/APV} = 3.11\times10^{-4}$,
78 $p_{gbz\text{-}vs\text{-}DNQX/APV} = 5.83\times10^{-4}$, post-hoc Mann-Whitney U [MWU] tests with False Discovery Rate
79 (FDR) p-value correction (see methods), $\alpha_{FDR} = 0.033$, $n_{control}$ = 8 mice, 4 cells, n_{gbz} = 7, 4,
80 $n_{DNQX/APV}$ = 7, 4). In contrast, eIPSCs were blocked by both gbz and DNQX/APV (Figure 1c;
81 $eIPSC_{control}$ = 148.82 [65.13/231.10] pA, $eIPSC_{gbz}$ = 1.00 [-0.98/2.50] pA, $eIPSC_{DNQX/APV}$ = 1.08
82 [0.56/3.15] pA, $p = 6.45\times10^{-4}$, KW test, $p_{Ctrl\text{-}vs\text{-}gbz} = 3.11\times10^{-4}$, $p_{Ctrl\text{-}vs\text{-}DNQX/APV} = 3.11\times10^{-4}$, $p_{gbz\text{-}vs\text{-}}$
83 $_{DNQX/APV} = 0.71$, post-hoc MWU tests, $n_{control}$ = 8, 4; n_{gbz} = 7, 4; $n_{DNQX/APV}$ = 7, 4), consistent with
84 a monosynaptic glutamatergic nature of the eEPSCs and a polysynaptic GABAergic nature of
85 the eIPSCs. Additionally, eIPSC onset was delayed relative to eEPSC onset by ~3 ms (Figure 1d;
86 mean ± standard error of the mean [s.e.m.]; $latency_{EPSC}$ = 7.65 ± 0.51 ms, $latency_{IPSC}$ = 10.72 ±
87 0.85 ms, $p = 0.023$, paired t-test, n = 8, 4) consistent with prior reports of polysynaptic
88 inhibitory circuits in BLA[26-28].

89 Two main archetypal circuit motifs mediate polysynaptic inhibition: feedforward and
90 feedback inhibition[16]. In order to distinguish these motifs, we recorded from BLA PNs in

91 response to a stimulus train of five pulses to the LEC at 20 Hz. If eIPSCs were the result of FFI
92 alone, we would expect to see little to no AP activity in BLA PNs in response to stimulation.
93 However, if the eIPSCs were a result of combined feedforward and feedback inhibition, we
94 would expect to see the PNs fire in response to LEC stimulation. Recording from BLA PNs in
95 current clamp (-60 mV), we found they rarely fired in response to stimulation (Figure 1e,f;
96 0.00 [0.00/0.07] APs/stimulus). These data suggest LEC stimulation preferentially drives FFI
97 in BLA PNs.

98 To determine whether our experimental setup recapitulates LEC suppression of BLA
99 PNs, as found *in vivo*[15], we tested the effect of gbz on the firing of BLA PNs in response to LEC
100 stimulation (Figure 1e-g). However, $GABA_A$ receptor antagonism might increase the firing of
101 BLA PNs by depolarizing the PNs via a blockade of spontaneous or tonic inhibition. To control
102 for this possibility, we maintained the membrane voltage (V_m) of the PNs at -60 mV
103 throughout the experiments (Fig. 1g; $V_{m\text{-control}}$ = -60.07 [-60.55/-59.79], $V_{m\text{-gbz}}$ = -60.91 [-
104 61.68/-59.34], p = 0.38, Wilcoxon signed rank [WSR] test, n = 8, 3). gbz mediated blockade of
105 FFI led to a significant increase in PN firing in response to LEC stimulation (Figure 1e, f;
106 $APs/stimulus_{control}$ = 0.00 [0.00/0.07], $APs/stimulus_{gbz}$ = 0.26 [0.03/0.64], p = 0.031, WSR
107 test, n = 8, 3). These findings confirm that the horizontal slice preparation contained a
108 functionally complete LEC → BLA circuit supporting their use for the study of FFI.

109 **Cell type specificity of the LEC → BLA circuit**

110 We performed minimal stimulation experiments in the LEC → BLA circuit using whole cell
111 patch clamp electrophysiology to examine putative unitary synaptic events between
112 neurons[13,29]. Briefly, stimulation intensity was tuned to a threshold intensity where LEC
113 stimulation elicits eEPSCs in BLA neurons with a ~50% success rate and an all-or-none
114 amplitude (Supplementary Figure 1); at lower stimulation intensities eEPSCs do not occur. As

115 these eEPSCs likely represent the response of the neuron to the activation of a single LEC
116 neuron, this method provides a reliable measure of the unitary EPSC (uEPSC) between the
117 stimulated and recorded neurons[13,29]. To identify dendritic-targeting Sst^+ and perisomatic-
118 targeting PV^+ INs in acute brain slices, we generated Sst-tdTomato and PV-tdTomato mouse
119 lines by crossing Sst-*ires*-Cre and PV-*ires*-Cre mice to *Ai9* tdTomato reporter line. Sst-
120 tdTomato mice showed reliable labeling of Sst^+ cells and low overlap with PV^+ cells and PV-
121 tdTomato mice showed reliable labeling of PV^+ cells and low overlap with Sst^+ cells
122 (Supplementary figure 2). When minimally stimulating LEC we found that, whereas only a
123 subset of BLA PNs (12/24 cells) and Sst^+ INs (16/35 cells) responded with EPSCs, nearly every
124 PV^+ IN (15/16 cells) responded to the stimulation with an eEPSC (Figure 2a). DNQX and D-
125 APV abolished eEPSCs in all cell types, confirming the glutamatergic nature of the response
126 (Supplementary Figure 1).

127 Next, we compared putative uEPSCs across cell types (Figure 2b-d). We found that the
128 uEPSC amplitude was larger in Sst^+ and PV^+ INs compared to PNs (Figure 2e; Sst^+ = 44.81
129 [34.39/55.80] pA, PV^+ = 43.03 [39.02/58.51] pA, PN = 18.90 [15.57/26.22] pA, $p = 5.55 \times 10^{-4}$,
130 KW test, $p_{Sst\text{-}vs\text{-}PV} = 0.95$, $p_{Sst\text{-}vs\text{-}PN} = 6.45 \times 10^{-4}$, $p_{PV\text{-}vs\text{-}PN} = 8.30 \times 10^{-4}$, post-hoc MWU tests,
131 $\alpha FDR = 0.033$, $n_{Sst} = 16, 8$, $n_{PV} = 15, 5$, $n_{PN} = 12, 8$). Additionally, we found the uEPSC kinetics
132 were faster in the INs compared to PNs (Figure 2f; 20%-80% risetime: Sst^+ = 0.42 [0.36/0.52]
133 ms, PV^+ = 0.51 [0.41/0.65] ms, PN = 1.56 [1.04/2.03] ms, $p = 1.66 \times 10^{-5}$, KW test, $p_{Sst\text{-}vs\text{-}PV}$ =
134 0.29, $p_{Sst\text{-}vs\text{-}PN} = 2.16 \times 10^{-5}$, $p_{PV\text{-}vs\text{-}PN} = 1.56 \times 10^{-4}$, post-hoc MWU tests, $\alpha FDR = 0.033$; τ_{Decay}:
135 Sst^+ = 2.38 [1.67/3.80] ms, PV^+ = 1.95 [1.57/3.23] ms, PN = 8.68 [6.30/10.70] ms, $p = 2.18 \times$
136 10^{-5}, KW test, $p_{Sst\text{-}vs\text{-}PV} = 0.40$, $p_{Sst\text{-}vs\text{-}PN} = 3.21 \times 10^{-4}$, $p_{PV\text{-}vs\text{-}PN} = 1.26 \times 10^{-5}$, post-hoc MWU
137 tests, $\alpha FDR = 0.033$, $n_{Sst} = 16, 8$, $n_{PV} = 15, 5$, $n_{PN} = 12, 8$). Finally, we found no differences
138 between cell types in uEPSC latency or jitter (Figure 2g; latency: $Sst^+ = 8.66 \pm 0.56$ ms, PV^+ =

139 7.72 ± 0.45 ms, PN = 8.67 ± 0.48 ms, p = 0.32, one-way ANOVA; jitter: Sst^+ = 1.14 ± 0.17 ms,
140 PV^+ = 1.35 ± 0.17 ms, PN = 1.40 ± 0.26 ms, p = 0.60, one-way ANOVA, n_{Sst} = 16, 8, n_{PV} = 15, 5,
141 n_{PN} = 12, 8). Together with our data demonstrating that BLA PNs rarely fire in response to LEC
142 stimulation (Figure 1e, f), the statistically indistinguishable low jitters are consistent with a
143 monosynaptic connection between LEC projection neurons and BLA Sst^+ INs, PV^+ INs, and
144 PNs[30].

145 Since minimal stimulation likely reports the response of a BLA neuron to a single
146 upstream LEC neuron[13,29], we can use threshold stimulation intensity as an indirect measure of
147 convergence of LEC projection neurons onto different BLA cell types. If threshold stimulation
148 is lower for one BLA neuronal population compared to the others, it would follow that
149 convergence of LEC inputs onto that cell type is likely greater relative to the other populations
150 as it requires the activation of fewer LEC neurons. We found that threshold intensity was lower
151 for the Sst^+ INs compared to other cell types (Figure 2h; Sst^+ = 17.40 [5.01/64.00] μA×ms, PV^+
152 = 114.00 [30.00/160.00] μA×ms, PN = 273.00 [89.00/544.00] μA×ms, $p = 3.33 \times 10^{-4}$, KW
153 test, $p_{Sst\text{-}vs\text{-}PV}$ = 0.0047, $p_{Sst\text{-}vs\text{-}PN} = 3.83 \times 10^{-4}$, $p_{PV\text{-}vs\text{-}PN}$ = 0.092, post-hoc MWU tests, αFDR =
154 0.033, n_{Sst} = 16, 8, n_{PV} = 15, 5, n_{PN} = 12, 8).

155 Taken together, these data demonstrate that LEC stimulation leads to large and fast
156 unitary currents in BLA Sst^+ and PV^+ INs and small and slow unitary currents in BLA PNs.
157 Finally, although Sst^+ and PV^+ INs display equivalent uEPSCs, the finding that Sst^+ INs have a
158 lower threshold stimulation intensity compared to PV^+ INs and PNs suggest that LEC afferents
159 may have a greater functional convergence onto BLA Sst^+ compared to PV^+ INs.

160 **A fast spiking phenotype distinguishes BLA Sst^+ INs targeted by LEC afferents.**

161 Though little is known about BLA Sst+ INs, they appear to have diverse electrophysiological
162 properties *ex vivo*[9,31] and responses to stimuli *in vivo*[9,32], suggesting Sst may be expressed by a
163 broad range of GABAergic IN subtypes, similar to cortex[16]. Only a subset of Sst+ INs responded
164 to cortical stimulation raising the question whether these cells represented a distinct cell type.
165 To address this hypothesis, we ran an unsupervised cluster analysis using Ward's method[33]
166 based on 15 membrane properties from 78 Sst+ INs. Applying Thorndike's procedure[34]
167 suggested two distinct clusters (Groups I and II). A large majority of Sst+ INs that responded to
168 cortical stimulation clustered into Group I (13/16 cells) whereas a large majority of non-
169 responsive Sst+ INs clustered into Group II (15/19 cells) (Figure 3a). To better understand what
170 membrane properties best distinguished Group I and II Sst+ INs, we used decision tree analysis
171 which returned AP halfwidth as the most salient parameter for cluster separation (Figure 3b).
172 Finally, we used an additional predictive modeling technique, the random forest method. Like
173 decision tree analysis, the random forest method returned AP halfwidth as the most salient
174 parameter for defining BLA Sst+ INs (Supplementary Figure 3).

175 Having observed two subpopulations of Sst+ INs, we compared membrane properties
176 across Group I and II Sst+ INs and PV+ INs (Figure 3c-e, Supplementary Figure 4,
177 Supplementary Table 1). These data show that Group I Sst+ and PV+ INs differed from Group II
178 Sst+ INs in a subset of membrane properties such as AP halfwidth and maximum firing rate.
179 The membrane properties of Group I Sst+ and PV+ INs are consistent with a FS phenotype
180 typically seen in cortical, hippocampal, and BLA PV+ INs[16,35] (though see ref. 36, 37 for
181 examples of FS Sst+ INs in cortex) that is characterized by the ability to fire high frequency
182 trains of brief APs[16]. Taken together, the membrane properties of BLA Sst+ and PV+ INs reveal
183 two distinct subpopulations of Sst+ INs that are readily distinguished at the biophysical level by
184 their FS phenotype and at the functional circuit level by synaptic responses to cortical

185 stimulation. For clarity, we refer to the Group I and II Sst$^+$ INs as FS and non-fast spiking
186 (nFS) Sst$^+$ INs, respectively.

187 **LEC afferents specifically recruit FS Sst$^+$ INs to fire APs**

188 BLA Sst$^+$ INs have lower threshold stimulation intensity compared to PV$^+$ INs and PNs (Figure
189 2h). Since these data suggest a higher rate of convergence of LEC afferents onto Sst$^+$ compared
190 to PV$^+$ INs, we wanted to test the hypothesis that LEC input to BLA may preferentially recruit
191 Sst$^+$ over PV$^+$ INs. To do this, we recorded from BLA Sst$^+$ and PV$^+$ INs in current clamp at rest
192 and stimulated LEC with five pulses at 20 Hz. The stimulation intensity was set to the
193 empirically derived threshold stimulation for BLA PNs (defined as the median PN threshold
194 stimulation; 273 μA×ms; Figure 2h) allowing us us to determine how BLA INs respond when
195 LEC activity is sufficient to ensure that PNs receive input. We found that stimulation led to
196 robust spiking in BLA Sst$^+$ INs whereas PV$^+$ INs rarely fired (Figure 4a, b; APs/stimulus: Sst$^+$ =
197 0.93 [0.78/1.01], PV$^+$ = 0.00 [0.00/0.003], p = 0.016, MWU test, n_{Sst} = 8, 3, n_{PV} = 9, 3).

198 To probe the underlying mechanisms of the preferential spiking of Sst$^+$ INs, we utilized
199 two additional measures: resting V_m (V_{rest}) and subthreshold EPSP (stEPSP) amplitude. We
200 found that V_{rest} was more depolarized in Sst$^+$ compared to PV$^+$ INs (Figure 4c; V_{rest}: Sst$^+$ = -
201 59.24 ± 2.01 mV, PV$^+$ = -72.76 ± 5.14 mV, p = 0.034, unpaired t-test, n_{Sst} = 8, 3, n_{PV} = 9, 3).
202 Because individual INs displayed variability in the number of APs/stimulus, each IN would
203 have a different number of stEPSPs. Therefore, we compared both the distribution of all
204 stEPSP amplitudes and the mean cellular stEPSP amplitudes across Sst$^+$ and PV$^+$ INs.
205 Regardless of the analysis method, we found that evoked stEPSPs were larger in Sst$^+$ compared
206 to PV$^+$ INs (Figure 4d; $p = 2.19 \times 10^{-21}$, Kolmogorov-Smirnov (KS) test, n_{Sst} = 161 events, n_{PV} =
207 779 events; p = 0.030, MWU test, n_{Sst} = 5, 3, n_{PV} = 8, 3). Thus, the data show that two distinct

208 mechanisms appear to underlie the recruitment of BLA Sst$^+$ INs by LEC afferents: Sst$^+$ INs are
209 more depolarized at rest compared to PV$^+$ INs, and, despite the concomitant decrease in the
210 driving force through glutamate receptors, the magnitude of evoked stEPSPs was greater in
211 Sst$^+$ compared to PV$^+$ INs. Finally, when we classified the Sst$^+$ INs from this experiment
212 (Figure 3a), we found that all but one (7/8 cells) were FS Sst$^+$ INs, consistent with our finding
213 that LEC afferents appear to selectively target FS cells among the Sst$^+$ INs.

214 Taken together with the data in Figures 2 and 3, these data show that LEC stimulation
215 leads to synaptic responses in BLA FS Sst$^+$ INs, PV$^+$ INs, and PNs but not in nFS Sst$^+$ INs.
216 Although Sst$^+$ and PV INs have equivalent unitary events following LEC stimulation, the
217 responses of these cell types to LEC input diverge in important ways. Specifically, Sst$^+$ INs have
218 a lower threshold stimulation intensity compared to PV$^+$ INs, and Sst$^+$ INs have greater stEPSP
219 amplitudes and are more likely to fire in response to PN threshold stimulation of LEC
220 compared to PV$^+$ INs. These findings suggest that LEC afferents to BLA have a greater
221 functional convergence onto FS Sst$^+$ INs compared to PV$^+$ INs and raise the question whether
222 they are involved in BLA FFI.

223 **FS Sst$^+$ INs mediate BLA FFI**

224 To test whether Sst$^+$ or PV$^+$ INs provide cortically evoked FFI onto BLA PNs, we generated Sst-
225 hM4Di and PV-hM4Di mice by crossing the Sst-*ires*-Cre or PV-*ires*-Cre mice to the ROSA-
226 hM4Di-mCitrine mice. These mice selectively express hM4Di in Sst$^+$ (Sst-hM4Di) or PV$^+$ (PV-
227 hM4Di) INs. hM4Di is an inhibitory chemogenetic receptor that, when bound to its ligand
228 clozapine-*N*-oxide (CNO), activates the $G_{i/o}$ signaling cascade to hyperpolarize and block
229 neurotransmitter release from neurons[38,39]. To validate the efficacy of the Sst-hM4Di and PV-
230 hM4Di mouse lines, we patched onto BLA mCitrine$^+$ neurons and recorded V_m in current
231 clamp (I_{hold} = 0 pA). Application of 10 μM CNO reduced V_m of mCitrine$^+$ neurons in both lines

232 (Figure 5a; $\Delta V_{m\text{-}Sst}$ = -7.18 ± 2.21 mV, $\Delta V_{m\text{-}PV}$ = -9.43 ± 3.16 mV, p_{Sst} = 0.017, p_{PV} = 0.031, one-
233 sample t-test, n_{Sst} = 7, 4, n_{PV} = 6, 3). Thus, we used the Sst-hM4Di and PV-hM4Di mice to
234 selectively hyperpolarize Sst^+ and PV^+ INs.

235 To assess the role of Sst^+ and PV INs in BLA FFI, we stimulated LEC and recorded
236 eEPSCs and eIPSCs in BLA PNs using Sst-hM4Di and PV-hM4Di mice before and after bath
237 application of CNO (10 μM). To determine the effect of IN inactivation on FFI we quantified
238 two measures: eIPSC amplitude and inhibition-excitation balance (I/E balance). We defined
239 I/E balance as the eIPSC amplitude for each cell normalized to its eEPSC amplitude. We
240 examined this measure in addition to eIPSC amplitude to control for potential differences
241 across cells with regards to the number of excitatory inputs to BLA activated by LEC
242 stimulation. Consistent with the disynaptic nature of LEC-driven FFI in BLA (Figure 1), LEC
243 stimulation elicited an eIPSC that was significantly delayed relative to the eEPSC in BLA PNs
244 in both Sst-hM4Di and PV-hM4Di mice in control conditions and in the presence of CNO
245 (Figure 5b; Sst-hM4Di: $latency_{Sst\text{-}EPSC\text{-}Ctrl}$ = 7.01 ± 0.26 ms, $latency_{Sst\text{-}IPSC\text{-}Ctrl}$ = 8.57 ± 0.38 ms,
246 $latency_{Sst\text{-}EPSC\text{-}CNO}$ = 6.77 ± 0.26 ms, $latency_{Sst\text{-}IPSC\text{-}CNO}$ = 8.57 ± 0.31 ms, $p_{Sst\text{-}Ctrl}$ = 0.0018, $p_{Sst\text{-}}$
247 $_{CNO}$ = 8.80 × 10^{-4}, paired t-tests, n_{Sst} = 13, 6; PV-hM4Di: $latency_{PV\text{-}EPSC\text{-}Ctrl}$ = 7.28 [5.89/7.41]
248 ms, $latency_{PV\text{-}IPSC\text{-}Ctrl}$ = 9.52 [7.40/10.30] ms, $latency_{PV\text{-}EPSC\text{-}CNO}$ = 6.87 ± 0.27 ms, $latency_{PV\text{-}IPSC,}$
249 $_{CNO}$ = 9.32 ± 0.66 ms, $p_{PV\text{-}Ctrl}$ = 2.44 × 10^{-4}, WSR test, $p_{PV\text{-}CNO}$ = 0.0042, paired t-test, n_{PV} = 13,
250 7). Importantly, these data indicate that hM4Di expression or CNO application does not alter
251 the ability of LEC stimulation to drive FFI. When we perfused CNO to inactivate the different
252 IN subtypes, CNO reduced eIPSC amplitude and I/E balance in PNs from Sst-hM4Di mice by
253 30.2% and 40.2% respectively but had no effect on either measure in PNs from PV-hM4Di
254 mice (Figure 5c, d; Sst-hM4D$_i$: $IPSC_{Sst\text{-}Ctrl}$ = 223.27 [131.10/439.99] pA, $eIPSC_{Sst\text{-}CNO}$ = 155.88
255 [108.44/388.54] pA, I/E $balance_{Sst\text{-}Ctrl}$ = 3.34 [2.50/4.78], I/E $balance_{Sst\text{-}CNO}$ = 1.95 [1.41/2.46],

256 $p_{Sst\text{-}IPSC}$ = 0.040, $p_{Sst\text{-}IE}$ = 0.013, WSR tests, n_{Sst} = 13, 6; PV-hM4Di: $IPSC_{PV\text{-}Ctrl}$ = 238.06 ±
257 45.08 pA, $eIPSC_{PV\text{-}CNO}$ = 201.87 ± 28.20 pA, I/E $balance_{PV\text{-}Ctrl}$ = 3.53 ± 0.65, I/E $balance_{PV\text{-}CNO}$
258 = 3.63 ± 0.67, $p_{PV\text{-}IPSC}$ = 0.35, $p_{PV\text{-}IE}$ = 0.85, paired t-tests, n = 13, 7). Finally, demonstrating the
259 effects of Sst^+ and PV^+ IN inactivation were specific to the FFI, bath application of CNO had no
260 effect on eEPSCs in either mouse line (Supplementary Figure 5).

261 To control for off-target effects of CNO[40], we repeated the experiments in wildtype (WT)
262 littermates of Sst-hM4Di and PV-hM4Di mice. In WT littermates, LEC stimulation elicited the
263 delayed EPSC-IPSC pairing consistent with FFI (Figure 5b; $latency_{EPSC\text{-}Ctrl}$: 6.63 [6.41/7.17] ms,
264 $latency_{IPSC\text{-}Ctrl}$: 9.27 [7.39/10.14] ms, $latency_{EPSC\text{-}CNO}$: 6.75 ± 0.30 ms, $latency_{IPSC\text{-}CNO}$: 8.50 ±
265 0.42 ms, p_{Ctrl} = 0.0024, WSR test, p_{CNO} = 0.0012, paired t-test, n= 12, 6), and CNO application
266 had no effect on LEC-driven excitation or FFI in BLA (Figure 5e; Supplementary Figure 5;
267 $IPSC_{Ctrl}$ = 172.29 [135.00/313.01] pA, $IPSC_{CNO}$ = 189.68 [91.11/550.64] pA, I/E $balance_{Ctrl}$ =
268 1.64 [0.83/7.30], I/E $balance_{CNO}$ = 2.34 [1.31/5.13], p_{IPSC} = 0.73, p_{IE} = 0.68, WSR tests, n = 12,
269 6). Taken together with our data demonstrating that LEC afferents selectively synapse onto FS
270 Sst^+ INs among the Sst^+ IN subtypes (Figures 2-3), these data show that FS Sst^+, but not PV^+ or
271 nFS Sst^+, INs mediate LEC-driven FFI in BLA.

272 **FS Sst+ INs control BLA plasticity**

273 A major role of BLA FFI is to gate the induction of LTP[8,10,11]. Because FS Sst^+ INs mediate LEC
274 evoked FFI, we hypothesized that Sst^+, but not PV^+, INs would gate the induction of LTP at the
275 synapse between the cortical afferents and BLA PNs. To test this hypothesis, we modified a
276 Hebbian-pairing LTP protocol used previously to study plasticity at synapses between cortical
277 afferents and PNs of the lateral amygdala[24]. This protocol pairs EPSPs with postsynaptic APs.
278 Each AP is followed by brief, sustained postsynaptic depolarization (25 ms) that induces

279 backpropagating Ca^{2+} spikes[25] and is necessary for LTP to occur[24]. For our initial experiments,
280 we wanted to validate that this pairing protocol would induce LTP at the LEC to BLA synapse.
281 To do this, we stimulated LEC and recorded eEPSCs in BLA PNs in the presence of 5 μM gbz to
282 block $GABA_A$ receptors. Unexpectedly, pairing presynaptic and postsynaptic activity in the
283 presence of gbz induced a bidirectional plasticity (see Methods for how direction and
284 significance of plasticity was determined). In 7 of 8 PNs, pairing induced a long-term change in
285 eEPSC amplitude (Figure 6a; LTP: 145.39 ± 8.17 % baseline eEPSC amplitude, n = 4, 4; LTD:
286 63.63 ± 4.55 %, n = 3, 3).

287 Next, we wanted to test the hypothesis that the Sst^+ INs gate LTP at the LEC to BLA
288 synapse. We reasoned that if we inactivate the INs subtype that gates plasticity, the number of
289 PN responding with long-term plastic changes when we stimulate with the pairing protocol
290 should increase. We repeated plasticity experiments with the Sst-hM4Di and PV-hM4Di mice
291 and included 10 μM CNO in the bath to selectively inactivate either cell type. Inactivating Sst^+
292 INs while stimulating PNs with the pairing protocol induced a bidirectional plasticity in 7 of 8
293 neurons (Figure 6b; LTP: 141.79 ± 7.33 %, n = 3, 3; LTD: 58.82 ± 10.90 %, n = 4, 3). However,
294 when we ran PNs through the pairing protocol while inactivating PV^+ INs, the majority of PNs
295 did not undergo plastic changes. Specifically, in 6 of 8 PNs there was no effect on eEPSC
296 amplitude (Figure 6c; No plasticity PNs: 93.33 ± 5.97, n = 6, 4). Finally, we compared the
297 proportion of PNs undergoing long-term plastic changes across our three conditions ($GABA_A$
298 receptor blockade, Sst^+ IN inactivation, and PV^+ IN inactivation) and found that a significantly
299 greater proportion of neurons underwent long-term plastic changes when we blocked all
300 $GABA_A$ receptor or selectively inactivated Sst^+ INs compared to PV^+ IN inactivation (Figure 6d;
301 Proportion plastic: WT mice + gbz = 0.88, Sst-hM4Di + CNO = 0.88, PV-hM4Di + CNO =
302 0.25; $p_{WT\text{-}vs\text{-}Sst} = 1.00$, $p_{WT\text{-}vs\text{-}PV} = 0.012$, $p_{Sst\text{-}vs\text{-}PV} = 0.012$, X^2 test, αFDR = 0.033, $n_{WT} = 8$, 6,

303 n_{Sst} = 8, 7, n_{PV} = 8, 7). Thus, we found that Sst$^+$, but not PV$^+$, INs gate plasticity at the LEC to
304 BLA synapse.

305 Discussion

306 In summary, our data show that a previously unreported subpopulation of FS Sst$^+$ INs
307 mediates LEC-driven FFI to gate plasticity in BLA (Figure 7). Although LEC afferents synapse
308 onto both PV$^+$ and FS Sst$^+$ INs, only FS Sst$^+$ INs fired in response to LEC activity. Inactivation
309 of Sst$^+$, but not PV$^+$, INs led to a reduction in FFI and to plastic changes at the LEC → BLA
310 synapse that mirrored those seen during $GABA_A$ receptor blockade. Our findings are consistent
311 with prior experiments in BLA indicating that FFI gates plasticity onto PNs[8,10,11], experiments
312 suggesting Sst$^+$ INs form the anatomical circuit underlying FFI[17,18], and the demonstration that
313 Sst$^+$ IN activity *in vivo* regulates BLA-dependent learning[32]. Finally, these data illuminate a
314 circuit mechanism for the feedforward inhibitory control mediated by entorhinal afferents onto
315 BLA PNs[15].

316 Specifically, our data show that FS Sst$^+$ INs mediate FFI to gate BLA plasticity. Similar
317 to cortex[16], BLA Sst$^+$ INs are a heterogenous population with diverse firing properties[9,31].
318 Accordingly, cluster analysis revealed two distinct subpopulations of Sst$^+$ INs that could be
319 distinguished based on their membrane properties, most notably AP halfwidth. Interestingly,
320 the two clusters also separated the populations of Sst$^+$ INs based on whether they displayed a
321 synaptic response to LEC stimulation: 81.3% of Sst$^+$ INs with a synaptic response were
322 classified as FS and 79.4% of Sst$^+$ without a response were nFS. Although canonically, PV$^+$ INs
323 are thought to be synonymous with FS INs, our data indicate that, at least in BLA, this is not
324 the case. In BLA, our data reveal two functionally distinct populations of FS INs can be
325 separated based on PV or Sst expression. Further, taken together with recent descriptions of FS
326 Sst$^+$ INs in cortex[16,36,37], we argue that a FS phenotype is insufficient to classify an IN solely as

327 PV$^+$. Thus, FS Sst$^+$ INs appear to be a biophysically and functionally distinct class of Sst$^+$ INs
328 with that mediate FFI to gate plasticity at LEC inputs onto BLA PNs. Whether the findings of
329 the LEC → BLA circuit extend to other afferents to BLA is an important question. Prior studies
330 suggest they likely do (see Supplementary Discussion); nevertheless, future experiments are
331 necessary to test this premise.

332 The findings of the present study differ substantially from previous reports on FFI in
333 cortex and hippocampus. In these structures, which share similar neuronal subtypes with
334 BLA[1], PV$^+$, and not Sst$^+$, INs mediate FFI[14,16]. Why would this be the case? We believe that our
335 finding that FS Sst$^+$ INs are the circuit mechanism underlying BLA plasticity holds the key to
336 answering this question. In cortex and hippocampus, FFI exerts control over the *temporal*
337 *fidelity of AP output* of PNs[12,13] whereas in BLA, FFI plays a critical role in exerting control over
338 the *plasticity* of PNs[8,10,11]. Consistent with the role of FFI in cortex and hippocampus, the major
339 circuit role of the perisomatic PV$^+$ INs in cortex, hippocampus, and BLA is to regulate the AP
340 output of PNs[12,14,16,41]. Conversely, BLA Sst$^+$ INs primarily target the dendrites of PNs[32,42].
341 Interestingly, the major circuit role of dendritic targeting INs is to regulate the local calcium
342 flux in dendrites[19-21], placing this cell type in prime position to exert control of synaptic
343 plasticity. This circuit role of dendritic targeting INs is consistent with the role of BLA FFI and
344 with our findings that FS Sst$^+$ INs in BLA mediate FFI to control plasticity. Additionally, BLA
345 PV$^+$ INs are readily recruited by low levels of activity in local PNs[43] and are connected via
346 electrical synapses synchronizing their activity across groups of local PV$^+$ INs[35]. Thus, PV$^+$ INs
347 are in a prime position to provide feedback and lateral inhibition to control BLA output
348 whereas FS Sst$^+$ INs are in a prime position to regulate plasticity via FFI. Together, the
349 inhibitory networks would work in concert to finetune patterns of BLA activity to allow animals
350 to learn about and react to stimuli. Our results illuminate an important point: archetypal
351 circuit motifs that reappear across brain regions may be mediated by different types of neurons

352 in these brain areas depending on the functional role of the local circuit motif, but the
353 functional role of the neuronal subtypes appears to remain consistent.

354 BLA has been implicated in a variety of neuropsychiatric diseases ranging from anxiety
355 to addiction[1,2]. Specifically, anxiety is thought to involve abberrant BLA-dependent learning[1].
356 Our finding that FS Sst^+ IN mediated FFI is the circuit mechanism gating BLA plasticity
357 suggests that *in vivo* manipulation of this cell population may have therapeutic potential.

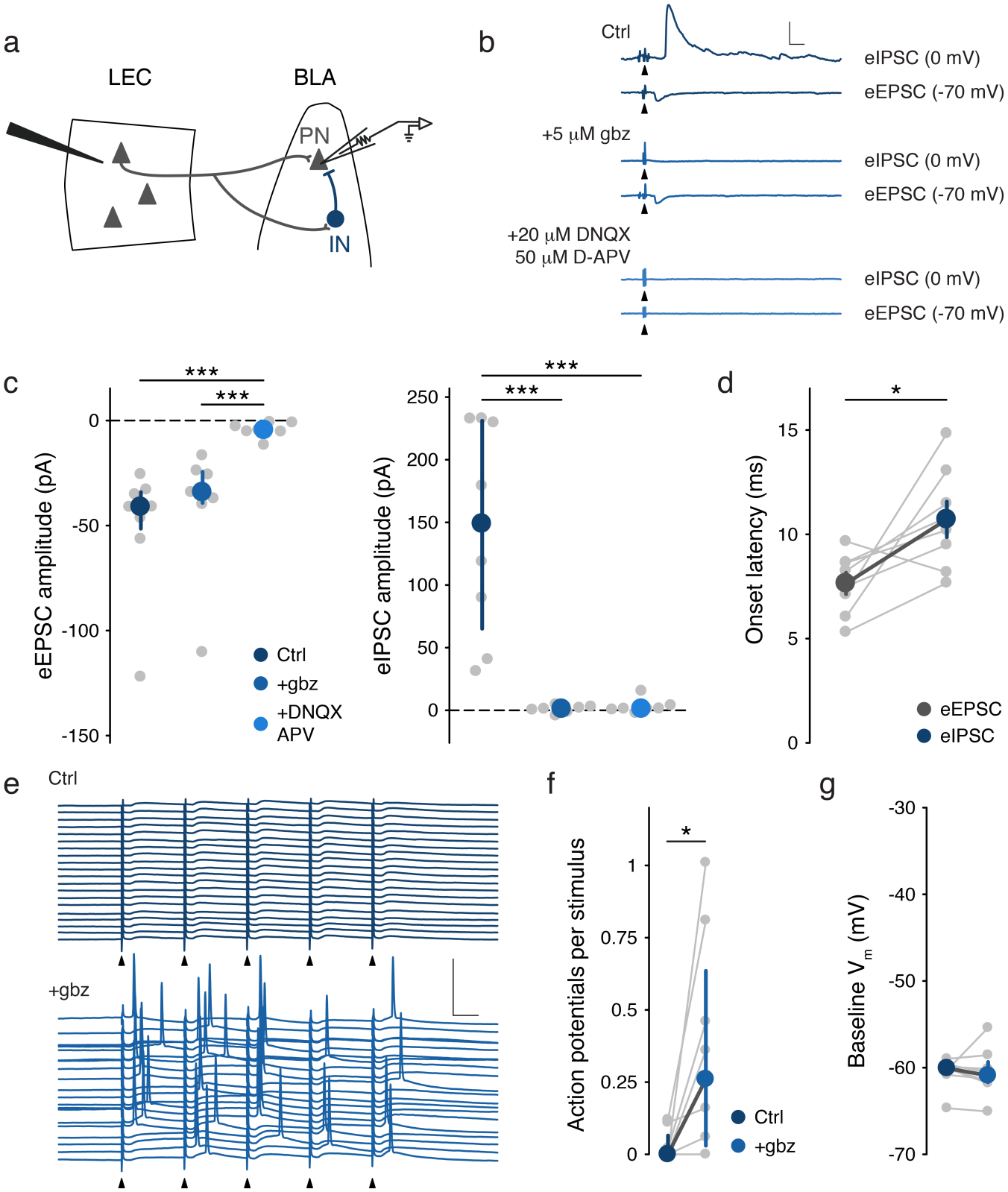

Figure 1. LEC afferents preferentially mediate FFI in BLA PNs. **(a)** Experimental schematic **(b)** Mean traces of eEPSCs and eIPSCs in a BLA PN in response to LEC stimulation (control;

gbz, 5 μM; DNQX, 20 μM, D-APV, 50 μM). Arrowheads: stimulation (artifacts truncated). **(c)** eEPSCs blocked by DNQX/APV (KW test: $p = 6.72\times10^{-4}$; $n_{control} = 8, 4$, $n_{gbz} = 7, 4$, $n_{DNQX/APV} = 7, 4$). eIPSCs blocked by gbz and DNQX/APV (KW test: $p = 6.45\times10^{-4}$; $n_{control} = 8, 4$, $n_{gbz} = 7, 4$, $n_{DNQX/APV} = 7, 4$). **(d)** Onset latency of eIPSC is delayed relative to the eEPSC (paired t-test: $p = 0.023$, n = 8, 4). **(e)** 20 voltage traces from a BLA PN (control; gbz) in response to 5× stimulation of LEC at 20 Hz. Arrowheads: stimulation. **(f)** $GABA_A$ receptor blockade increases AP firing in BLA PNs in response to LEC stimulation (WSR test: $p = 0.031$, n = 8, 3). **(g)** Baseline V_m did not differ between control and gbz (WSR test: $p = 0.38$, n = 8, 3). Statistics in **d** presented in color (mean ± s.e.m). Statistics in **c**, **f**, **g** presented in color (median and interquartile range [IQR]). Individual data points: ●. *$p < 0.05/\alpha_{FDR}$ (where applicable), **$p < 0.01$, ***$p < 0.001$. Please see Results for post-hoc test p values.

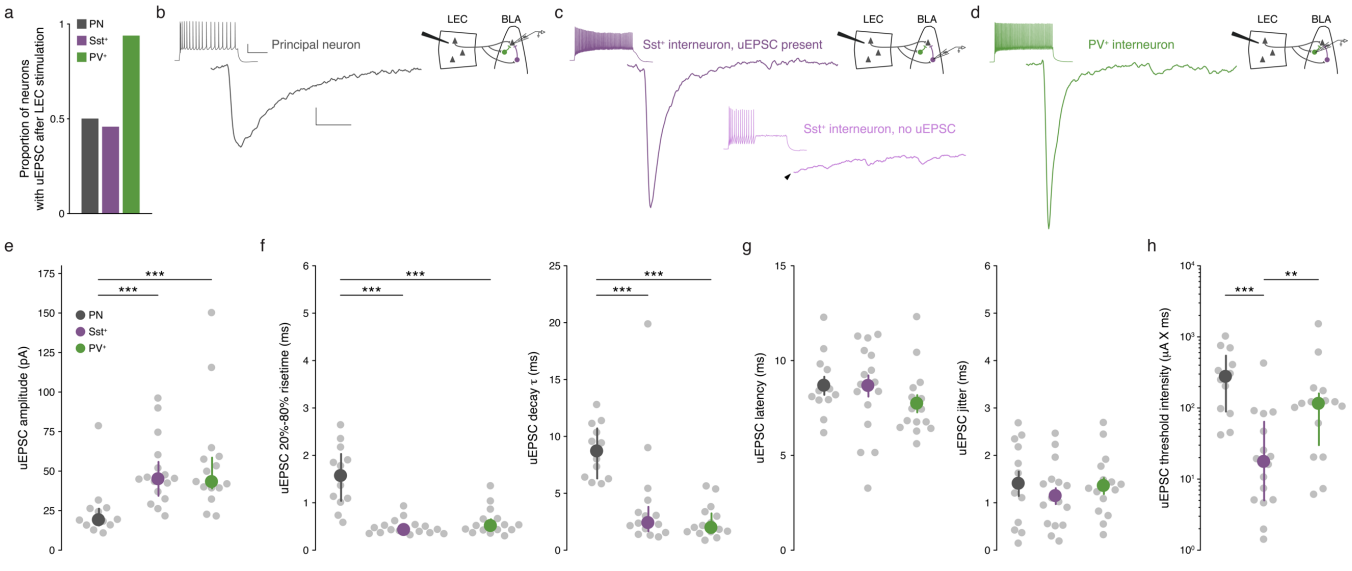

Figure 2. Cell type specificity of the LEC → BLA circuit. **(a)** Proportion of neurons with detectable uEPSCs following LEC stimulation. **(b)-(d)** Center: Mean traces of uEPSC successes from a representative PN **(b)**, Sst⁺ IN **(c)**, PV⁺ IN **(d)**. Left, top: maximal firing to a current injection.. **(c)** Lower center: Mean trace of lack of response in Sst⁺ IN without a detectable uEPSC. Arrowhead: truncated stimulus artifact. **(e)** uEPSC amplitude is larger in Sst⁺/PV⁺ INs compared to PNs (KW test: $p = 5.55 \times 10^{-4}$). **(f)** Left: uEPSC 20%-80% risetime is faster in Sst⁺/PV⁺ INs compared to PNs (KW test: $p = 1.66 \times 10^{-5}$). Right: uEPSC τ_{Decay} is faster in Sst⁺/PV⁺ INs compared to PNs (KW test: $p = 2.18 \times 10^{-5}$). **(g)** Left: uEPSC latency does not differ across cell types (one-way ANOVA: $p = 0.32$). Right: uEPSC jitter does not differ across cell types (one-way ANOVA: $p = 0.60$). **(h)** uEPSC threshold intensity is lower for Sst⁺ INs (KW test: $p = 3.33 \times 10^{-4}$). Statistics in **g** mean ± s.e.m. Statistics in **e**, **f**, **h** median and IQR. Individual data points: ●. $^{*}p < 0.05/\alpha_{FDR}$ (where applicable), $^{**}p < 0.01$, $^{***}p < 0.001$. For all statistical tests: $n_{Sst} = 16, 8$, $n_{PV} = 15, 5$, $n_{PN} = 12, 8$. Please see Results for post-hoc test p values.

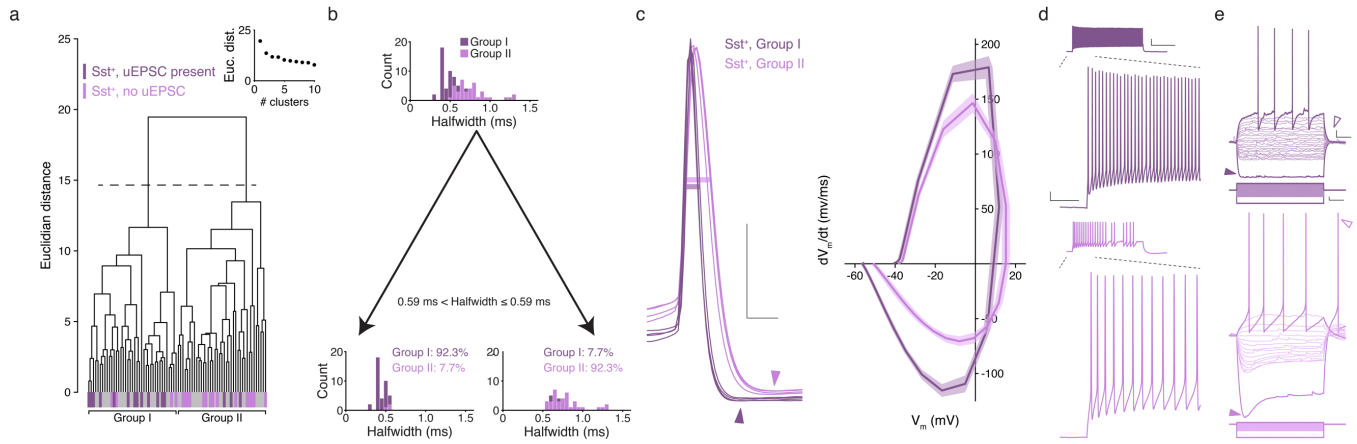

Figure 3. A FS phenotype distinguishes BLA Sst+ INs targeted by LEC. **(a)** Unsupervised clustering analysis revealed two clusters of Sst+ INs. Majority of Sst+ INs with a uEPSC present following LEC stimulation cluster in Group I (13/16). Majority of Sst+ INs with no response to LEC stimulation cluster in Group II (15/19). **(b)** Decision tree analysis; AP halfwidth (0.59 ms) best separates Group I and II Sst+ INs. **(c)** Left: APs of representative Group I (▬) and II (▬) Sst+ INs at rheobase. Halfwidth: (■,■) . AHP latency: (▲,▲). Scale bars: 20 mV, 1 ms. Right: Phase plot of Group I and Group II Sst+ INs shows rate of voltage change for Group I and II APs at rheobase. Mean trace: (▬,▬). s.e.m.: (■,■). n_{SstI} = 39, 15, n_{SstII} = 39, 12. **(d)** Maximum AP firing from representative Group I (▬) and II (▬) Sst+ INs at rheobase. Scale bars, top inset: 20 mV, 200 ms; middle: 5 mV, 50 ms. **(e)** Voltage responses of Group I and II Sst+ INs. (▬,▬) to -200 pA and rheobase current injections. (▬,▬) intermediate current injections were used to determine membrane resistance (-100 pA to sweep immediately before rheobase, Δ10 pA each sweep). Note lack of sag, rebound AP in Group I Sst+ IN (sag: ▲, ▲; rebound AP: Δ, Δ). Scale bars: 5 mV, 100 ms; 50 pA, 100 ms.

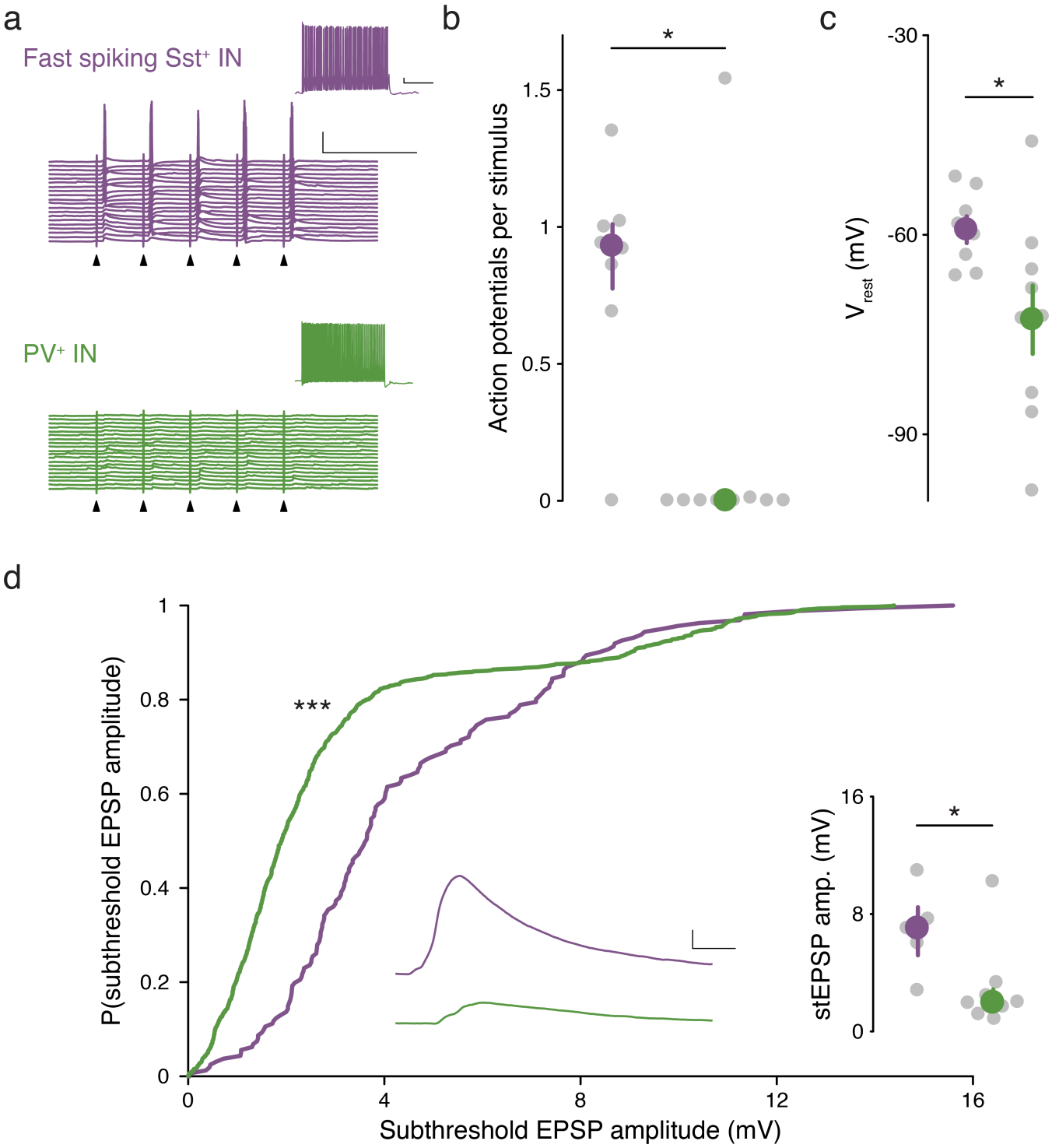

Figure 4. LEC afferents preferentially drive spiking in Sst+ INs. **(a)** Representative Sst+ (top) and PV+ (bottom) responses to LEC stimulation at 20 Hz (stimulation artifacts: ▲; scale bars: 25 mV, 100 ms). Insets show maximal firing frequency for the representative IN in response to a square current pulse (scale bars: 5 mV, 200 ms). **(b)** Sst+ INs fire more APs per stimulus

407 compared to PV+ INs. MWU test: $p = 0.016$, $n_{Sst} = 8$ cells, 3 mice, $n_{PV} = 9$ cells, 3 mice **(c)** Sst+

408 INs that respond to LEC stimulation have a more depolarization V_{rest} compared to PV+ INs.

409 Unpaired t-test: $p = 0.034$, $n_{Sst} = 8$ cells, 3 mice, $n_{PV} = 9$ cells, 3 mice **(d)** Cumulative

410 probability distribution of all stEPSPs. Inset, middle: mean stEPSP from representative

411 neurons in **(a)** (Sst+: ▬, PV+: ▬, scale bars: 1 mV, 5 ms). KS test: $p = 2.19 \times 10^{-21}$, $n_{Sst} = 161$

412 events, $n_{PV} = 779$ events; MWU test: $p = 0.030$, $n_{Sst} = 5$ cells, 3 mice, $n_{PV} = 8$ cells, 3 mice

413 Individual data points: ●. Summary statistics in **c** presented in color as mean ± s.e.m.

414 Summary statistics in **b**, **d** (inset) presented in color as median with errors bars displaying the

415 IQR. *$p < 0.05$, **$p < 0.01$, ***$p < 0.001$.

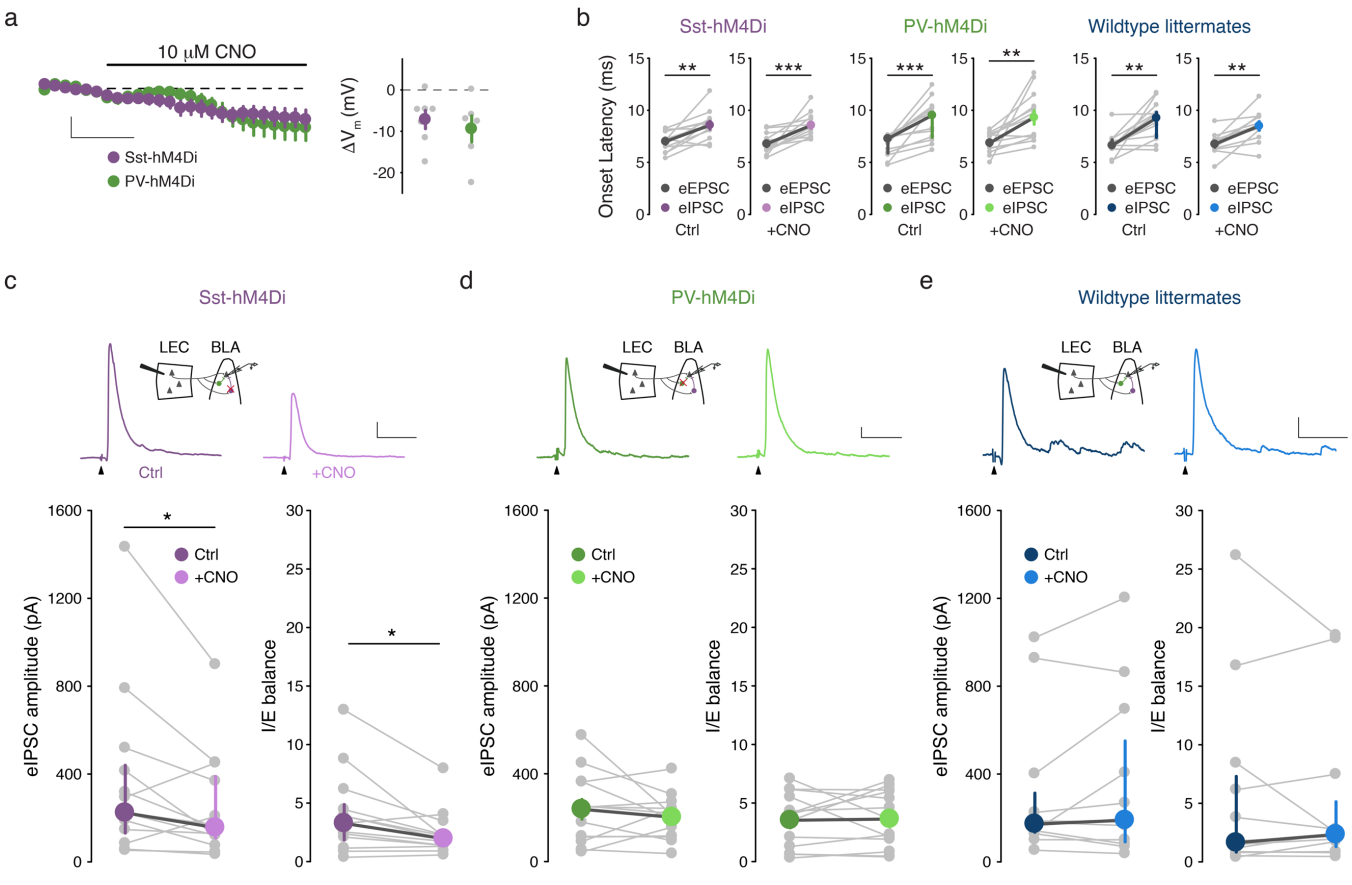

Figure 5. Sst⁺ INs mediate FFI. **(a)** Left: Effect of CNO on V_m (scale bars: 5 mV, 3 min). Right: CNO hyperpolarizes mCitrine⁺ cells in both mouse lines (p_{Sst} = 0.017, p_{PV} = 0.031, one-sample t-test, n_{Sst} = 7, 4, n_{PV} = 6, 3). **(b)** eIPSC is delayed relative to eEPSC in all mouse lines (paired t-tests: $p_{Sst\text{-}Ctrl}$ = 0.0018, $p_{Sst\text{-}CNO}$ = 8.80 × 10^{-4}, $p_{PV\text{-}CNO}$ = 0.0042, $p_{WT\text{-}CNO}$ = 0.0012; WSR tests: $p_{PV\text{-}Ctrl}$ = 2.44 × 10^{-4}, $p_{WT\text{-}Ctrl}$ = 0.0024; n_{Sst} = 13, 6, n_{PV} = 13, 7, n_{WT} = 12, 6). **(c)-(e)** Effect of CNO on FFI in Sst-hM4Di **(c)**, PV-hM4Di **(d)**, and WT littermates **(e)**. Top: Experimental schema, eIPSC traces with and without CNO. Arrowheads: stimulation artifacts (truncated). Scale bars: **(c)** 100 pA, 50ms; **(d)**, 25 pA, 50ms; **(e)**, 50 pA, 50 ms. Bottom: **(c)** Sst⁺ IN inactivation reduced FFI (WSR tests: p_{IPSC} = 0.040, p_{IE} = 0.013, n = 13, 6). **(d)** No effect of PV⁺ IN inactivation (paired t-tests: p_{IPSC} = 0.35, p_{IE} = 0.85, n = 13, 7). **(e)** No effect of CNO in WT littermates (WSR tests: p_{IPSC} = 0.73, p_{IE} = 0.68, n = 12, 6). Individual data points: ● . Summary statistics in **a**, **b** (Sst-hM4Di both conditions, PV-hM4Di CNO condition, WT

429 littermates CNO condition), and **d** in color as mean ± s.e.m. Summary statistics in **b** (PV-

430 hM4Di and WT littermates control conditions), **c**, and **e** in color as median with IQR. *p <

431 0.05, **p < 0.01, ***p < 0.001.

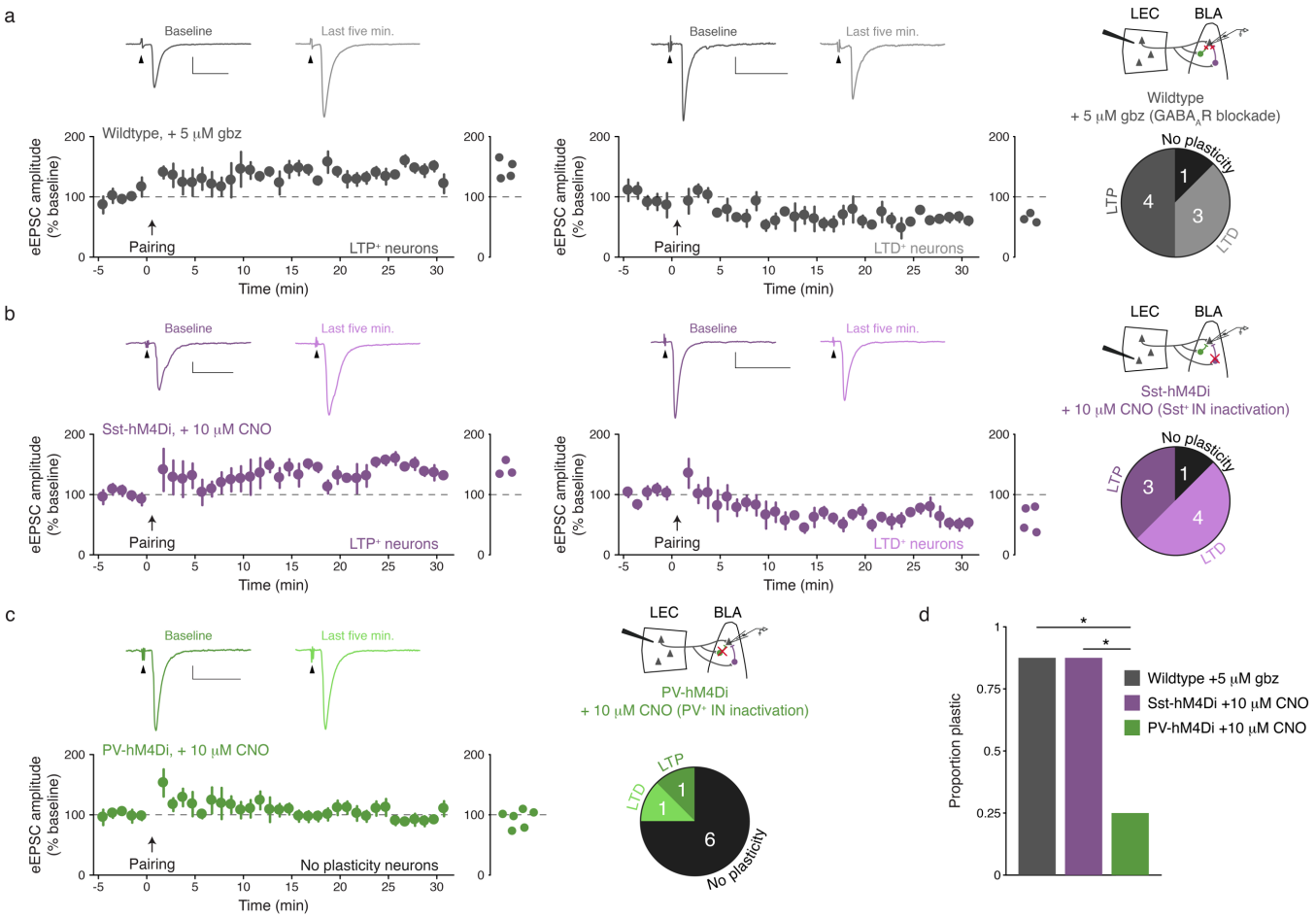

Figure 6. BLA Sst⁺ INs gate plasticity. **(a)**, **(b)**, **(c)** Bottom: Plot of eEPSC (% baseline) amplitude as a function of time; data displayed as mean ± s.e.m. Scatter plot to the right of eEPSC time course shows eEPSC amplitude (% baseline) in the last five minutes. Left **(a)**, **(b)**, PNs that underwent significant LTP. Left **(c)**, PNs with no significant plasticity. Middle **(a)**, **(b)**, PNs that underwent significant LTD. Top: Mean eEPSC traces from a representative PN, baseline period and last five minutes (arrowheads: stimulation artifact [truncated]; scale bars, **a**, LTP: 50 pA, 40 ms; LTD: 20 pA, 40 ms; **b**, LTP: 25 pA, 30 ms; LTD: 50 pA, 40 ms; **c**, 20 pA, 40 ms). Right, top: experimental schema. Right, bottom: pie chart of eEPSC amplitude change induced by the pairing protocol. **(a)** PNs recorded from WT mice in gbz (n_{total} = 8, 7; n_{LTP} = 4, 4; n_{LTD} = 3, 3). **(b)** PNs recorded from Sst-hM4Di mice with CNO (n_{total} = 8, 7; n_{LTP} = 3, 3; n_{LTD} = 4 cells, 3). **(c)** PNs recorded from PV-hM4Di mice with CNO (n_{total} = 8, 6; $n_{no\text{-}plasticity}$ = 6, 4).

(d) Note, significantly more cells undergo long-term plastic changes during $GABA_A$ receptor blockade and Sst^+ IN inactivation compared to PV^+ IN inactivation (X^2 test: $p_{WT\text{-}vs\text{-}Sst} = 1.00$, $p_{WT\text{-}vs\text{-}PV} = 0.012$, $p_{Sst\text{-}vs\text{-}PV} = 0.012$, $\alpha FDR = 0.033$, $n_{WT} = 8$, 6, $n_{Sst} = 8, 7$, $n_{PV} = 8, 7$).

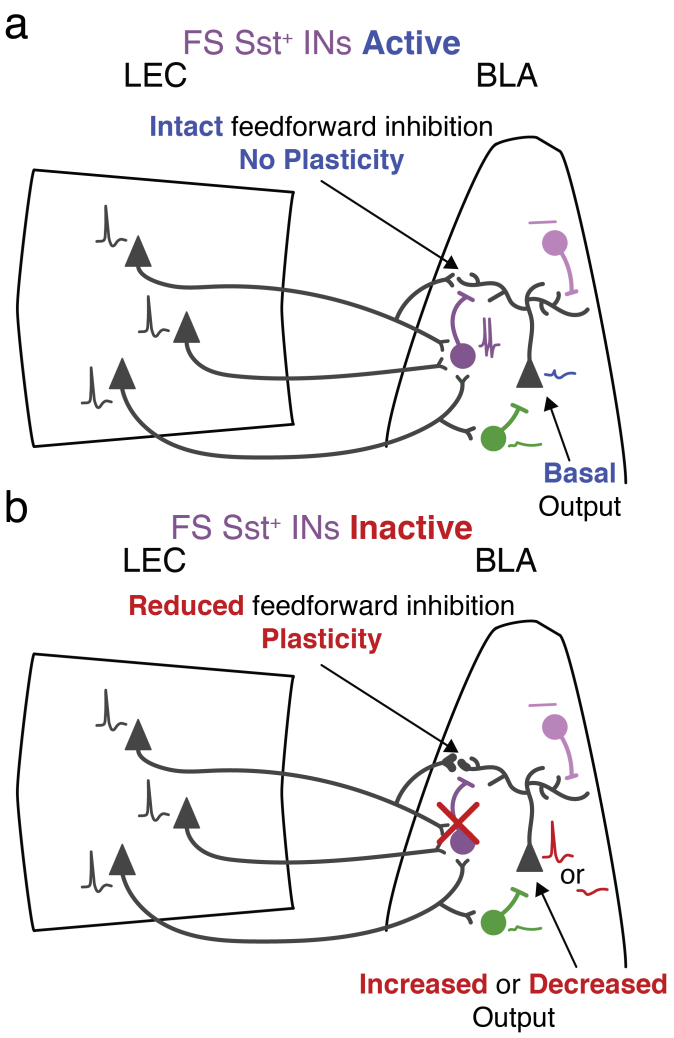

Figure 7. Schematic of findings. FS Sst+ INs (●) fire APs in response to LEC input. nFS Sst+ INs (●) do not respond to LEC input. PV+ INs (●)respond with a subthreshold excitatory response to LEC input. **(a)** When FS Sst+ IN mediated FFI is intact, BLA PNs will output their basal response to LEC input. **(b)** Inactivation of FS Sst+ IN removes the feedforward inhibitory control over BLA PNs, allowing them to undergo plastic changes.

454 **References**

455 1. Duvarci, S. & Paré, D. Amygdala microcircuits controlling learned fear. *Neuron* **82,** 966–
456 980 (2014).

457 2. Janak, P. H. & Tye, K. M. From circuits to behaviour in the amygdala. *Nature* **517,** 284–
458 292 (2015).

459 3. Quirk, G. J., Repa, C. & LeDoux, J. E. Fear conditioning enhances short-latency auditory
460 responses of lateral amygdala neurons: Parallel recordings in the freely behaving rat.
461 *Neuron* **15,** 1029–1039 (1995).

462 4. Beyeler, A. *et al.* Divergent Routing of Positive and Negative Information from the
463 Amygdala during Memory Retrieval. *Neuron* **90,** 348–361 (2016).

464 5. McKernan, M. G. & Shinnick-Gallagher, P. Fear conditioning induces a lasting
465 potentiation of synaptic currents in vitro. *Nature* **390,** 607–611 (1997).

466 6. Nabavi, S. *et al.* Engineering a memory with LTD and LTP. *Nature* **511,** 348–352 (2014).

467 7. Kim, W. B. & Cho, J.-H. Encoding of Discriminative Fear Memory by Input-Specific LTP
468 in the Amygdala. *Neuron* **95,** 1129–1146.e5 (2017).

469 8. Bissière, S., Humeau, Y. & Lüthi, A. Dopamine gates LTP induction in lateral amygdala
470 by suppressing FFI. *Nat Neurosci* **6,** 587–592 (2003).

471 9. Krabbe, S., Gründemann, J. & Lüthi, A. Amygdala Inhibitory Circuits Regulate
472 Associative Fear Conditioning. *Biol. Psychiatry* **83,** 800–809 (2018).

10. Tully, K., Li, Y., Tsvetkov, E. & Bolshakov, V. Y. Norepinephrine enables the induction of associative long-term potentiation at thalamo-amygdala synapses. *Proc Natl Acad Sci USA* **104,** 14146–14150 (2007).

11. Bazelot, M. *et al.* Hippocampal Theta Input to the Amygdala Shapes FFI to Gate Heterosynaptic Plasticity. *Neuron* **87,** 1290–1303 (2015).

12. Pouille, F. & Scanziani, M. Enforcement of temporal fidelity in pyramidal cells by somatic feed-forward inhibition. *Science* **293,** 1159–1163 (2001).

13. Gabernet, L., Jadhav, S. P., Feldman, D. E., Carandini, M. & Scanziani, M. Somatosensory integration controlled by dynamic thalamocortical feed-forward inhibition. *Neuron* **48,** 315–327 (2005).

14. Glickfeld, L. L. & Scanziani, M. Distinct timing in the activity of cannabinoid-sensitive and cannabinoid-insensitive basket cells. *Nat Neurosci* **9,** 807–815 (2006).

15. Lang, E. J. & Paré, D. Similar inhibitory processes dominate the responses of cat lateral amygdaloid projection neurons to their various afferents. *Journal of Neurophysiology* **77,** 341–352 (1997).

16. Tremblay, R., Lee, S. & Rudy, B. GABAergic Interneurons in the Neocortex: From Cellular Properties to Circuits. *Neuron* **91,** 260–292 (2016).

17. Smith, Y., Paré, J. F. & Paré, D. Differential innervation of parvalbumin-immunoreactive interneurons of the basolateral amygdaloid complex by cortical and intrinsic inputs. *J. Comp. Neurol.* **416,** 496–508 (2000).

493 18. Unal, G., Paré, J.-F., Smith, Y. & Paré, D. Cortical inputs innervate calbindin-
494 immunoreactive interneurons of the rat basolateral amygdaloid complex. *J. Comp.*
495 *Neurol.* **522,** 1915–1928 (2014).

496 19. Miles, R., Tóth, K., Gulyás, A. I., Hájos, N. & Freund, T. F. Differences between somatic
497 and dendritic inhibition in the hippocampus. *Neuron* **16,** 815–823 (1996).

498 20. Chiu, C. Q. *et al.* Compartmentalization of GABAergic inhibition by dendritic spines.
499 *Science* **340,** 759–762 (2013).

500 21. Müllner, F. E., Wierenga, C. J. & Bonhoeffer, T. Precision of Inhibition: Dendritic
501 Inhibition by Individual GABAergic Synapses on Hippocampal Pyramidal Cells Is
502 Confined in Space and Time. *Neuron* **87,** 576–589 (2015).

503 22. Weisskopf, M. G., Bauer, E. P. & LeDoux, J. E. L-type voltage-gated calcium channels
504 mediate NMDA-independent associative long-term potentiation at thalamic input
505 synapses to the amygdala. *Journal of Neuroscience* **19,** 10512–10519 (1999).

506 23. Bauer, E. P., Schafe, G. E. & LeDoux, J. E. NMDA receptors and L-type voltage-gated
507 calcium channels contribute to long-term potentiation and different components of fear
508 memory formation in the lateral amygdala. *J. Neurosci.* **22,** 5239–5249 (2002).

509 24. Humeau, Y. *et al.* Dendritic spine heterogeneity determines afferent-specific Hebbian
510 plasticity in the amygdala. *Neuron* **45,** 119–131 (2005).

511 25. Humeau, Y. & Lüthi, A. Dendritic calcium spikes induce bi-directional synaptic plasticity
512 in the lateral amygdala. *NP* **52,** 234–243 (2007).

513 26. Arruda-Carvalho, M. & Clem, R. L. Pathway-selective adjustment of prefrontal-amygdala
514 transmission during fear encoding. *J. Neurosci.* **34,** 15601–15609 (2014).

515 27. Hübner, C., Bosch, D., Gall, A., Lüthi, A. & Ehrlich, I. Ex vivo dissection of
516 optogenetically activated mPFC and hippocampal inputs to neurons in the basolateral
517 amygdala: implications for fear and emotional memory. *Front Behav Neurosci* **8,** 64
518 (2014).

519 28. Lucas, E. K., Jegarl, A. M., Morishita, H. & Clem, R. L. Multimodal and Site-Specific
520 Plasticity of Amygdala Parvalbumin Interneurons after Fear Learning. *Neuron* **91,** 629–
521 643 (2016).

522 29. Kumar, S. S. & Huguenard, J. R. Properties of excitatory synaptic connections mediated
523 by the corpus callosum in the developing rat neocortex. *Journal of Neurophysiology* **86,**
524 2973–2985 (2001).

525 30. Doyle, M. W. & Andresen, M. C. Reliability of monosynaptic sensory transmission in
526 brain stem neurons in vitro. *Journal of Neurophysiology* **85,** 2213–2223 (2001).

527 31. Sosulina, L., Graebenitz, S. & Pape, H.-C. GABAergic interneurons in the mouse lateral
528 amygdala: a classification study. *Journal of Neurophysiology* **104,** 617–626 (2010).

529 32. Wolff, S. B. E. *et al.* Amygdala interneuron subtypes control fear learning through
530 disinhibition. *Nature* **509,** 453–458 (2014).

531 33. Ward, J. H. Hierarchical grouping to optimize an objective function. *Journal of the*
532 *American Statistical Association* **58,** 236–244 (1963).

533 34. Thorndike, R. L. Who belongs in the family? *Psychometrika* **18,** 267–276 (1953).

534 35. Woodruff, A. R. & Sah, P. Networks of Parvalbumin-Positive Interneurons in the
535 Basolateral Amygdala. *Journal of Neuroscience* **27,** 553–563 (2007).

536 36. Ma, Y., Hu, H., Berrebi, A. S., Mathers, P. H. & Agmon, A. Distinct subtypes of
537 somatostatin-containing neocortical interneurons revealed in transgenic mice. *J.*
538 *Neurosci.* **26,** 5069–5082 (2006).

539 37. Large, A. M., Kunz, N. A., Mielo, S. L. & Oswald, A.-M. M. Inhibition by Somatostatin
540 Interneurons in Olfactory Cortex. *Front. Neural Circuits* **10,** 62 (2016).

541 38. Armbruster, B. N., Li, X., Pausch, M. H., Herlitze, S. & Roth, B. L. Evolving the lock to fit
542 the key to create a family of G protein-coupled receptors potently activated by an inert
543 ligand. *Proc Natl Acad Sci USA* **104,** 5163–5168 (2007).

544 39. Stachniak, T. J., Ghosh, A. & Sternson, S. M. Chemogenetic synaptic silencing of neural
545 circuits localizes a hypothalamus→midbrain pathway for feeding behavior. *Neuron* **82,**
546 797–808 (2014).

547 40. Gomez, J. L. *et al.* Chemogenetics revealed: DREADD occupancy and activation via
548 converted clozapine. *Science* **357,** 503–507 (2017).

549 41. Woodruff, A. R. & Sah, P. Inhibition and Synchronization of Basal Amygdala Principal
550 Neuron Spiking by Parvalbumin-Positive Interneurons. *Journal of Neurophysiology* **98,**
551 2956–2961 (2007).

552 42. Muller, J. F., Mascagni, F. & McDonald, A. J. Postsynaptic targets of somatostatin-
553 containing interneurons in the rat basolateral amygdala. *J. Comp. Neurol.* **500,** 513–529
554 (2007).

555 43. Andrási, T. *et al*. Differential excitatory control of 2 parallel basket cell networks in
556 amygdala microcircuits. *PLoS Biol* **15,** e2001421 (2017).

557

558

559 **Methods**

560 ***Animals***

561 All experiments were conducted in accordance with protocols approved by the Institutional
562 Animal Care and Use Committee at the University of Colorado Anschutz Medical Campus. Slice
563 electrophysiology experiments were conducted on mice aged postnatal days 35-70.
564 Immunohistochemistry experiments were conducted on mice aged postnatal days 60-120.
565 Experiments were conducted on both male and female mice, and estrous samples were
566 collected from female mice used in experiments. The following mouse lines were used in the
567 experiments: C57Bl/6J (Jackson Lab #000664), Sst-tdTomato, PV-tdTomato, Sst-hM4Di, PV-
568 hM4Di, and wildtype littermates of the Sst-hM4Di and PV-hM4Di mice. Sst-tdTomato, PV-
569 tdTomato, Sst-hM4Di, and PV-hM4Di mouse lines were generated by crosses of Sst-*ires*-Cre
570 (Jackson Lab #013044) and PV-*ires*-Cre (Jackson Lab #008069) lines with either the Rosa-
571 CAG-LSL-tdTomato-WPRE (*Ai9*; Jackson Lab #007905) or the R26-hM4Di/mCitrine
572 (Jackson Lab # 026219) lines.

573 ***Acute slice preparation for electrophysiology***

574 Animals were first anesthetized with CO_2 and decapitated. Brains were quickly dissected and
575 placed in an ice-cold, oxygenated (95% O_2-5% CO_2) sucrose-based slicing solution (in mM:
576 sucrose, 45; glucose, 25; NaCl, 85; KCl, 2.5; NaH_2PO_4, 1.25; $NaHCO_3$, 25; $CaCl_2$, 0.5; $MgCl_2$, 7;
577 osmolality, 290-300 mOsm/kg). 300-400μm horizontal slices were obtained using a
578 vibratome (Leica Biosystems, Buffalo Grove, IL, USA). Slices were incubated in oxygenated
579 (95% O_2-5% CO_2) artificial cerebral spinal fluid (ACSF; in mM: glucose, 10; NaCl, 124; KCl, 2.5;
580 NaH_2PO_4, 1.25; $NaHCO_3$, 25; $CaCl_2$, 2; $MgCl_2$, 2; osmolality 290-300 mOsm/kg) at 36˚C for at
581 least 30 minutes. All reagents were purchased from Sigma-Aldrich (St. Louis, MO, USA).

582 ***Electrophysiology***

583 Slices were placed in a submerged slice chamber and perfused with ACSF heated to 32-37˚C.
584 Slices were visualized using a moving stage microscope (Scientifica: Uckfield, UK; Olympus:
585 Tokyo, Japan) equipped with 4× (0.10 NA) and 40× (0.80 NA) objectives, differential
586 interference contrast (DIC) optics, infrared illumination, LED illumination (CoolLED,
587 Andover, UK), a CoolSNAP EZ camera (Photometrics, Tuscon, AZ, USA), and Micro-Manager
588 1.4 (Open Imaging, San Francisco, CA, USA). Whole cell patch clamp recordings were made
589 using borosilicate glass pipettes (2.5-5.0 MΩ; King Precision Glass, Claremont, CA, USA) filled
590 with intracellular recording solution. For voltage clamp experiments on FFI a cesium
591 methanesulfonate (CsMe) based intracellular solution was used (in mM: CsMe, 120; HEPES,
592 10; EGTA, 0.5; NaCl, 8; Na-phosphocreatine, 10; QX-314, 1; MgATP, 4; Na_2GTP, 0.4; pH to 7.3
593 with CsOH; osmolality adjusted to approximately 290 mOsm/kg). For all remaining voltage
594 clamp experiments and for all current clamp experiments, a potassium gluconate based
595 intracellular solution was used (in mM: potassium gluconate, 135; HEPES, 10; KCl, 20; EGTA,
596 0.1; MgATP, 2; Na_2GTP, 0.3; pH to 7.3 with KOH; osmolality adjusted to approximately 295
597 mOsm/kg). Access resistance was monitored throughout the experiments and data were
598 discarded if access resistance exceeded 25 MΩ or varied by more than ± 20%. No junction
599 potential compensation was performed. Data were acquired with a Multiclamp 700B amplifier
600 and were converted to a digital signal with the Digidata 1440 digitizer using pCLAMP 10.6
601 software (Molecular Devices, Sunnyvale, CA). Data were sampled at 10 kHz and lowpass
602 filtered at 4 kHz. Offline, current data were filtered using a 3rd order Savistky-Golay filter with
603 a ± 0.5 ms window after access resistance was assessed. Mean traces were created by first
604 aligning all events by their point of maximal rise (postsynaptic currents) or by threshold (APs)
605 and then obtaining the mean of all events; mean subthreshold EPSPs were not aligned prior to
606 averaging. All reagents were purchased from Sigma-Aldrich (St. Louis, MO, USA) with the
607 exception of CsMe which was purchased from Acros Organics (NJ, USA).

508 ***Cell-type identification***

509 *Principal Neurons (PNs).* PNs were targeted based on their large, pyramidal-like soma.
510 Recordings were terminated if the physiology of the neuron was inconsistent with BLA PNs
611 (e.g. high membrane resistance, narrow AP halfwidth, large and fast spontaneous EPSCs).
512 *Interneurons (INs).* INs were targeted based on fluorescence in the SST-tdTomato, PV-
513 tdTomato, SST-hM4D$_i$, and PV-hM4D$_i$ mouse lines. A 470 nm LED was used to identify
514 mCitrine$^+$ INs in SST-hM4D$_i$ and PV-hM4D$_i$ mouse lines, and a 535 nm LED was used to
515 identify tdTomato$^+$ INs in the SST-tdTomato and PV-tdTomato mouse lines (CoolLED,
516 Andover, UK).

517 ***Pharmacology***

518 DNQX, D-APV, and gbz were purchased from Tocris Biosciences (Bristol, UK) and CNO was
519 purchased from Enzo Life Sciences (Farmingdale, NY). DNQX stock was made at 40 mM and
520 diluted to a final concentration of 20 μM in ACSF; D-APV stock was made at 50 mM and
521 diluted to a final concentration of 50 μM in ACSF; GBZ stock was made at 25 mM and diluted
522 to a final concentration of 5 μM in ACSF; and, CNO stock was made at 10 mM and diluted to a
523 final concentration of 10 μM in ACSF. All stocks were stored at -20°C and CNO was used
524 within one month of making the stock solution.

525 ***Electrophysiology experimental design***

526 *FFI, voltage clamp.* The LEC was stimulated using a bipolar stimulating electrode (FHC, Inc.,
527 Bowdoin, ME, USA). eEPSCs (V_{hold} = -70 mV) and eIPSCs (V_{hold} = 0 mV) were recorded from
528 BLA PNs in response to LEC stimulation. To assess the effects of different drugs on the eEPSCs
529 and eIPSCs, ACSF containing DNQX, D-APV, gbz, and/or CNO was perfused onto the slice for
530 five minutes prior to and continuously during the experiment. Effects of DNQX/APV and gbz
531 on eEPSCs and eIPSCs were recorded using in an unpaired design where some PNs were
532 recorded under control conditions and in the presence of DNQX/APV and gbz (given

533 sequentially with time for washout) whereas others were recorded under control conditions in
534 the presence of DNQX/APV or gbz. Effects of CNO on eEPSCs and eIPSCs were examined with
535 a paired design where all PNs were recorded in both control conditions and in the presence of
536 CNO.
537 *FFI, current clamp*. Membrane voltage of BLA PNs was recorded in response to 5 stimulations
538 of the LEC at 20 Hz. I_{hold} was adjusted such that V_{rest} of the PNs was approximately -60 mV. To
539 assess the role of $GABA_A$ receptor mediated inhibition on PN AP firing, gbz was perfused onto
540 the slice for five minutes prior to and continuously during the experiment.
541 *Current injections*. Membrane voltage of BLA neurons was recorded in current clamp in
542 response to a series of square hyperpolarizing and depolarizing current injections. Prior to
543 initiation of the series of current injections, V_m of the BL neurons was adjusted to
544 approximately -60 mV. Each cell was subjected to two series of 600 ms square current
545 injections: -100 pA to +100 pA at 10 pA intervals and -200 pA to +400 pA at 25 pA intervals.
546 The data collected in these experiments were used to determine active and passive membrane
547 properties of the neurons.
548 *Minimal stimulation*. eEPSCs (V_{hold} = -70 mV) were recorded in voltage clamp in BLA PNs,
549 Sst^+ INs, and PV^+ INs in response to LEC stimulation. Stimulation intensity was adjusted such
550 that LEC stimulation resulted in recorded eEPSCs having a success rate of approximately 50%
551 and an all-or-none amplitude response.
552 *Recruitment of BLA INs by LEC afferents*. The median stimulation intensity necessary to
553 observe putative uEPSCs in BLA PNs (273 μA × ms) was used as the empirically derived PN
554 threshold stimulation intensity. Membrane voltage responses of BLA Sst^+ and PV^+ INs were
555 recorded in current clamp in response to 5 stimulations of the LEC at 20 Hz at the empirically
556 derived PN threshold stimulation intensity.

557 *Pharmacological effects of CNO on membrane potential.* Membrane voltage of mCitrine+
558 neurons in BLA was recorded in the presence of 20 μM DNQX, 50 μM D-APV, and 5 μM GBZ.
559 To assess the effects of CNO on membrane potential, baseline V_m was allowed to stabilize and
560 was recorded for 3 minutes in the absence of CNO. Following recording of baseline V_m, ACSF
561 containing 10 μM CNO was perfused onto the slice and V_m was recorded for an additional 10
562 minutes. V_m was separated into 30 second bins. ΔV_m was defined as the difference in V_m
563 between the mean V_m during the 3 minutes of baseline recordings and the mean V_m during the
564 last 3 minutes of CNO application.
565 *IN control of BLA plasticity*. All experiments were done in acute slices from wildtype mice with
566 5 μM gbz in the bath or in acute slices from Sst-hM4Di/PV-hM4Di mice with 10 μM CNO in
567 the bath. eEPSCs were recorded (V_{hold} = -70 mV) in BLA PNs in response to 0.067 Hz
568 stimulation of LEC (4 stimuli/minute). After a 5 minute baseline of eEPSCs was recorded,
569 plasticity was induced (in current clamp, I_{hold} adjusted such that V_m was set to approximately -
570 70 mV) by pairing three APs (2 nA, 5 ms current injections) with three monosynaptic EPSPs
571 elicited by LEC stimulation at 33.3 Hz. LEC stimulation was timed such the EPSP was recorded
572 approximately 5-10 ms prior to AP induction. Immediately following each AP, V_m was
573 depolarized to > -40 mV for 25ms. This induction protocol was repeated 15 × at 0.2 Hz.
574 Following plasticity induction, eEPSCs were recorded in response to LEC stimulation at 0.05
575 Hz for 30 minutes. Experiments were terminated if plasticity induction did not occur within
576 approximately 10 minutes of achieving whole-cell configuration. Experiments were discarded if
577 eEPSC amplitude did not achieve a stable level post-induction (significantly deviation from the
578 middle 5 minutes compared to the last 5 minutes of the post-induction period as determined
579 by MWU test). This was done to ensure that changes in eEPSC amplitude were related to
580 plasticity induction and were not a confound of other phenomena. Our plasticity induction
581 protocol was based on prior studies examining plasticity at cortical inputs to BLA[24,25]. To

682 determine if plasticity occurred, we compared eEPSC amplitude in the 5 minutes prior to
683 induction to eEPSC amplitude in the last 5 minutes of the post-induction period using a MWU
684 for each cell. To correct for multiple comparisons (i.e. testing for a change in eEPSC amplitude
685 across every cell in each genotype), we utilized the False Discovery Rate (FDR) method[44] to
686 adjust the critical significance value from 0.05 to a FDR-corrected value. For the wildtype mice
687 with 5 μM gbz, α_{FDR} was set to 0.044; for Sst-hM4Di mice with 10 μM CNO, α_{FDR} was set to
688 0.044; for PV-hM4Di mice with 10 μM CNO, α_{FDR} was set to 0.013. We defined cells as
689 undergoing LTP if they had a significant increase in eEPSC amplitude from baseline to the last
690 5 minutes of the post-induction period; we defined cells as undergoing LTD if they had a
691 significant decrease in eEPSC amplitude from baseline to the last 5 minutes of the post-
692 induction period. For display purposes, eEPSC amplitude was normalized to the mean baseline
693 eEPSC amplitude, and eEPSCs were binned by the minute.

694 ***Definitions of electrophysiological parameters***

695 *eEPSC/eIPSC detection and amplitude.* eEPSCs (V_{hold} = -70 mV) were defined as negatively
696 deflecting postsynaptic events that exceeded the mean baseline current (500 ms before
697 stimulation) by 6× the median absolute deviation of the baseline current and that occurred
698 within 20 ms of the end of the electrical stimulus artifact. eIPSCs (V_{hold} = 0 mV) were defined
699 as positively deflecting postsynaptic events that exceeded the mean baseline current by 6× the
700 median absolute deviation of the baseline current and that occurred within 20 ms of the end of
701 the electrical stimulus artifact. To ensure that the detected eEPSCs/eIPSCs were related to the
702 stimulus, we subsampled 25% of the sweeps in the experiment (or 5 sweeps if the experiment
703 consisted of <20 sweeps) and found the maximal peak negative (eEPSC detection) or positive
704 (eIPSC detection) deflection from baseline in the 20 ms after the stimulus artifact in those
705 sweeps. Then, we found the median peak time for those sweeps and repeated the analysis over
706 all sweeps in the experiment with a detection threshold of 6× the median absolute deviation of

707 the baseline current and with a window set to ± 5 ms (eEPSC detection) or ± 7.5 ms (eIPSC
708 detection) around the median peak time. The amplitude of each eEPSC and eIPSC was defined
709 as the difference between the peak amplitude of the detected eEPSC or eIPSC and the mean
710 baseline current for that sweep. The eEPSC or eIPSC amplitude for each cell in an experiment
711 was defined as the mean of the amplitudes recorded from that cell (eEPSC/eIPSC successes
712 only; failures were not included in eEPSC/eIPSC amplitude calculation). Where eEPSC failure
713 amplitude is reported on a per sweep basis, it was defined as the maximal negative deflection
714 from the current trace within ± 5 ms of the mean current peak time for that cell. If all sweeps
715 in an experiment were eEPSC/eIPSC failures, the mean eEPSC/eIPSC amplitude was defined
716 as the maximal negative (eEPSC) or positive (eIPSC) deflection in the mean current trace that
717 occurred within 20 ms of the end of the electrical stimulus artifact.
718 *Success rate*. Success rate was defined as $\mathbf{100}\% \times \frac{n_{successful\ sweeps}}{n_{total\ sweeps}}$ where successful sweeps were
719 defined as sweeps where an eEPSC was detected.
720 *I/E balance*. I/E balance was defined as the ratio of eIPSC to eEPSC amplitude recorded in the
721 same neuron.
722 *eEPSC/eIPSC 20%-80% risetime*. 20%-80% risetime was defined as the time it took an eEPSC
723 or eIPSC to reach 80% of its peak amplitude from 20% of its peak amplitude. 20%-80%
724 risetime was calculated for each sweep unless obscured by a spontaneous event. The risetime
725 for each cell was defined as the mean of all risetimes recorded from that cell.
726 *eEPSC/eIPSC latency and jitter*. Latency of eEPSCs and eIPSCs was defined as the time
727 between the end of the electrical stimulation and the point of 20% rise for an eEPSC or eIPSC
728 as calculated for the 20%-80% risetime. The eEPSC or eIPSC latency for each cell was defined
729 as the mean of the latencies recorded from that cell. The eEPSC or eIPSC jitter for each cell was
730 defined as the standard deviation of the latencies recorded from that cell.

731 *eEPSC/eIPSC τ_{Decay}*. eEPSC τ_{Decay} was determined using a single exponential fit, $\boldsymbol{f(t) = Ae^{-t/\tau}}$.
732 eIPSC τ_{Decay} was defined as the weighted time-constant of IPSC decay. Briefly, a double
733 exponential fit, $\boldsymbol{f(t) = A_1e^{-t/\tau_1} + A_2e^{-t/\tau_2}}$, was used to obtain the parameters to determine the
734 weighted time-constant where $\tau_{\boldsymbol{weighted}} = (\tau_1\boldsymbol{A_1} + \tau_2\boldsymbol{A_2})/(\boldsymbol{A_1} + \boldsymbol{A_2})$. τ_{Decay} was calculated using
735 the mean eEPSC or eIPSC trace for a cell and corresponds to the time it takes to reach $\frac{1}{e} \times I_{max}$.
736 *Membrane resistance*. Membrane resistance was defined as the slope of the best fit line of the
737 I-V plot using the -100 pA to +100 pA (10 pA steps) series of current injections. Mean voltage
738 response to each current injection step was defined as the difference between baseline mean
739 membrane voltage (100 ms prior to current injection) and the mean membrane voltage during
740 the last 200 ms of the current injection. The I-V plot was constructed using all current steps
741 below rheobase.
742 *Maximum firing rate*. Maximum firing rate was defined as the inverse of the inter-spike
743 interval (ISI) during the first 200 ms of the most depolarizing current injection step before
744 attenuation of AP firing was observed. Max FR was calculated using the -200 pA to +400 pA
745 (25 pA steps) series of current injections.
746 *AP threshold*. AP threshold was defined as the voltage at which $\frac{dV}{dt}$ exceeded 20 V/s. AP
747 threshold was calculated at the rheobase sweep of the -200 pA to +400 pA (25 pA steps) series
748 of current injections.
749 *AP amplitude*. Amplitude of the AP was defined as the voltage difference between the peak of
750 the AP and its threshold potential. AP amplitude was calculated at the rheobase sweep of the -
751 200 pA to +400 pA (25 pA steps) series of current injections.
752 *AP halfwidth*. AP halfwidth was defined as the time between the half-amplitude point on the
753 upslope of the AP waveform to the half-amplitude point on the downslope of the AP waveform.

754 AP halfwidth was calculated at the rheobase sweep of the -200 pA to +400 pA (25 pA steps)
755 series of current injections.
756 *After-hyperpolarization potential (AHP) magnitude*. AHP magnitude was defined as the
757 difference between the most hyperpolarized membrane voltage of the AHP (occurring within
758 100 ms after AP threshold) and AP threshold. AHP magnitude and latency data were calculated
759 at the rheobase sweep of the -200 pA to +400 pA (25 pA steps) series of current injections.
760 ΔAHP data were calculated at the rheobase + 50 pA sweep of the -200 pA to +400 pA (25 pA
761 steps) series of current injections.
762 *AHP latency*. AHP latency was defined as the time from AP threshold and the peak of the AHP.
763 *ΔAHP*. ΔAHP was defined as the difference between the first and last AHP ($\boldsymbol{\Delta AHP = AHP_{last} -}$
764 $\boldsymbol{AHP_{first}}$).
765 *AP phase plot*. The AP phase plot was obtained by plotting the rate of change of the mean AP
766 for each cell from the rheobase sweep of the -200 pA to +400 pA (25 pA steps) series of current
767 injections as a function of the corresponding membrane voltage.
768 *Latency to first AP*. AP latency was defined as the time from the initiation of the current
769 injection to the peak of the first AP. AP latency was calculated at the rheobase sweep of the -
770 200 pA to +400 pA (25 pA steps) series of current injections.
771 *Firing rate adaptation ratio (FR adaptation)*. Firing rate adaptation was defined as the ratio
772 of the ISIs of the first and average of the last three APs, such that $\boldsymbol{Firing\ rate\ adaptation} =$
773 $\frac{\boldsymbol{ISI_{first}}}{\boldsymbol{meanISI_{last-3APs}}}$. Firing rate adaptation was calculated at the rheobase +50 pA sweep of the -200
774 pA to +400 pA (25 pA steps) series of current injections.
775 *AP broadening*. AP broadening was defined as the ratio of the AP halfwidths of the first two
776 APs ($\boldsymbol{Broadening} = \frac{\boldsymbol{halfwidth_{second}}}{\boldsymbol{halfwidth_{first}}}$). AP broadening was calculated at the rheobase +50 pA
777 sweep of the -200 pA to +400 pA (25 pA steps) series of current injections.

778 *AP amplitude adaptation*. AP amplitude adaptation was defined as the ratio of the AP
779 amplitude of the average of the last three APs and the first AP, such that
780 $\boldsymbol{AP\ amplitude\ adaptation} = \frac{\boldsymbol{meanAmplitude_{last-3APs}}}{\boldsymbol{Amplitude_{first}}}$. AP amplitude adaptation was calculated at
781 the rheobase +50 pA sweep of the -200 pA to +400 pA (25 pA steps) series of current
782 injections.
783 *Membrane decay τ*. Membrane decay τ was determined by using a single exponential fit,
784 $\boldsymbol{f(t)} = \boldsymbol{Ae^{-t/\tau}}$, to fit the change in V_m induced by a -100 pA sweep in the -200 pA to +400 pA
785 (25 pA steps) series of current injections. The time given by τ corresponds to the time it takes
786 to reach $\left(\mathbf{1} - \frac{\mathbf{1}}{\boldsymbol{e}}\right) \times \Delta V_{max}$.
787 *Hyperpolarization-induced sag*. Hyperpolarization-induced sag was calculated using the
788 equation, $\frac{\boldsymbol{V_{min} - V_{ss}}}{\boldsymbol{V_{min} - V_{bl}}} \times \mathbf{100}\%$, where V_{min} was defined as the most hyperpolarized membrane
789 voltage during the current injection, V_{ss} was defined as the mean steady-state membrane
790 voltage (last 200 ms of the current injection), and V_{bl} was defined as the mean baseline
791 membrane voltage (100 ms prior to current injection). Hyperpolarization-induced sag was
792 measured from the -200 pA current injection.
793 *Rebound spikes*. Rebound spikes were defined as the number of APs in the 500 ms following
794 the -200 pA current injection.
795 *APs per stimulus*. The number of APs per stimulus was defined as the number of APs occurring
796 within 50 ms ($\frac{\mathbf{1}}{\mathbf{20\ Hz}}$) of the stimulus.
797 V_{rest}. V_{rest} was defined as V_m (I_{hold} = 0 pA) during a 500 ms baseline prior to LEC stimulation
798 during the experiments testing the recruitment of BLA INs by LEC afferents.
799 *Subthreshold EPSP amplitude*. Subthreshold EPSP amplitude was defined as the maximal,
800 non-stimulus artifact, voltage deflection within 40 ms after LEC stimulation.
801 ***Immunohistochemistry***

302 *Histological validation of PV⁺ and Sst⁺ IN identity*. To perform the PV and Sst
303 immunostaining, mice (n = 3 Sst-tdTomato mice, 3 PV-tdTomato mice) were sacrificed and
304 transcardially perfused with ice cold 4% PFA (with 1.5% picric acid and 0.05% glutaraldehyde)
305 followed by 30% sucrose protection. After the brain sank, coronal BLA slices of 30 μm
306 thickness were obtained. Before application of blocking solution, slices were incubated for 30
307 minutes at room temperature with iFX-enhancer (Invitrogen, ThermoFisher Scientific,
308 Waltham, MA, USA). After blocking, the slices were incubated with either rat anti-Sst antibody
309 (1:100, MAB354, Millipore, Burlington, MA, USA) or guinea pig anti-PV antibody (1:500,
310 195004, Synaptic Systems, Göttingen, Germany) for at least 48 hours at 4°C. Then, a secondary
311 antibody of either donkey anti-rat or donkey anti-guinea pig Alexa Fluor 488 (1:500,
312 Invitrogen) was applied overnight at 4°C. The slices were imaged using a confocal laser
313 scanning microscope (TCS SP5II, Leica Application Suite, Leica Biosystems, Buffalo Grove, IL,
314 USA) with 10× 0.40 NA and 20× 0.70 NA dry objectives to determine the neuron identity.

315 ***Data analysis***

316 *Statistical analyses*. All data analysis (except decision tree and random forest analyses) were
317 performed offline using custom written MATLAB code. Normality of the data were assessed
318 using the Anderson-Darling test. For assessment of whether a single group differed from a
319 normal distribution centered around zero, a one-sample t-test was used. For a test between two
320 groups, a paired or unpaired t-test was used where appropriate. For tests between two groups
321 of non-normal data, a Mann-Whitney U test or Wilcoxon signed-rank test was used where
322 appropriate. For tests between three or more groups of normal data with one independent
323 variable, a one-way ANOVA was used with Tukey's post-hoc test to examine differences
324 between groups. A Kruskal-Wallis test was used to examine differences between three or more
325 groups of non-normal data with one independent variable. A Mann-Whitney U test was used as
326 a post-hoc test following a significant result in a Kruskal-Wallis test and was corrected for

327 multiple comparisons using the FDR method[44]. The critical significance value was set to α =
328 0.05 or was set to a FDR-corrected value (α_{FDR}) for multiple comparisons. All statistical tests
329 were two-tailed. Unless otherwise stated, experimental numbers are reported as n = x, y where
330 x is the number of neurons and y is the number of mice.
331 *Unsupervised cluster analysis.* Unsupervised cluster analysis using Ward's method[33] was used
332 to classify Sst$^+$ INs. Briefly, this method involves plotting each neuron in multidimensional
333 space where each dimension corresponds to a given parameter. For our data, we plotted each
334 Sst$^+$ IN in 15-dimensional space (where each dimension corresponds to a z-score
335 transformation of one of the 15 membrane properties obtained from the current injection
336 experiments; values were z-score transformed so that parameters with large values, e.g.
337 membrane resistance, would not influence the cluster analysis more than those with small
338 values, e.g. halfwidth). From here, the analysis proceeded along $n - 1$ stages where n is the
339 number of Sst$^+$ INs. At stage $n = 1$, the two closest cells in the 15-dimensional space are
340 grouped together. At subsequent stages, the closest cells are grouped together until only one
341 group of all objects remains. We determined the final number of clusters by using the
342 Thorndike procedure[34] where large distances between group centroids at one cluster stage
343 relative to other stages are indicative of significant differences between groups (see Figure 3a,
344 inset).
345 *Decision tree analysis.* Recursive partitioning analyses[45] were conducted in R (1.01.136). The R
346 package rpart[46] was used for recursive partitioning for classification. Decision trees were
347 plotted using rpart.plot package, and random seeds were set using the rattle package. Predicted
348 classes were determined from the unsupervised cluster analysis and were used to determine
349 important discriminating parameters. The model was internally cross validated with a nested
350 set of subtrees and the final model was selected as the subtree with the least misclassification
351 error. Individual decision trees can suffer from overfitting. Therefore, the input parameters of

the model were independently cross validated by bootstrapping 500 subsamples (without replacement and using random seeds). Each tree was pruned by choosing the complexity parameter with the lowest cross validated error. The mean correct prediction of the test set classifications (n = 20% of sample) by the pruned tree generated by modeling the training sets (n = 80% of sample) was 86.7%.

Random forest analysis. Supervised classification random forest was employed to reduce potential model overfitting. Random forest classification was conducted using the randomForest package in R[47]. Random forest classification employs random subsampling of both parameters and bootstrapped subsamples of the dataset (with replacement). 10,000 decision trees were generated, and the modal tree was used as the final classification model. An additional cross validation step was conducted by bootstrapping 80% of the initial sample to create the random forest model and tested against a subsample (n = 20% of sample; bootstrapped without replacement). The mean accuracy after 20 random forest runs was 92.8%. Gini impurity was calculated to determine parameter importance. Visualization of the frequency of individual samples falling within the same node across one run of the classification algorithm was obtained by calculating a proximity matrix for the samples and plotting it against the first two principle components.

Data display. Data visualizations were created in MATLAB and Adobe Illustrator. Normal data are presented as the mean ± s.e.m. Non-normal data are presented as the median with error bars extending along the interquartile range.

Data availability. Data and MATLAB code are available on request and will be made available on GitHub.

References (continued)

44. Curran-Everett, D. Multiple comparisons: philosophies and illustrations. *Am. J. Physiol. Regul. Integr. Comp. Physiol.* **279**, R1–8 (2000).

45. Breiman, L., Friedman, J., Stone, C. J. & Olshen, R. A. *Classification and Regression Trees*. (Wadsworth).

46. Therneau, T. & Atkinson, B. rpart: Recursive Partitioning and Regression Trees. R package version 4.1-13 https://CRAN.R-project.org/package=rpart

47. Liaw, A. & Wiener, M. Classification and Regression by randomForest. *R News* **2**, 18-22.